

1 **Unravelling the origins and P-T-t evolution of the**
2 **allochthonous Sobrado unit (Órdenes complex, NW**
3 **Iberia) using combined U-Pb titanite, monazite and zircon**
4 **geochronology and REE geochemistry**

5 José Manuel Benítez-Pérez^{1,3}, Pedro Castiñeiras², Juan Gómez-Barreiro^{3(*)}, José R.
6 Martínez Catalán³, Andrew Kylander-Clark⁴, Robert Holdsworth⁵

7
8

9 ¹Centro de Ciências e Tecnologias Nucleares. Instituto Superior Técnico. Universidad de Lisboa. Estrada
10 Nacional 10 (km 139,7), 2695-066, Bobadela LRS, Portugal

11 ²Departamento de Mineralogía y Petrología. Facultad de Ciencias Geológicas, Universidad Complutense
12 de Madrid. C/ José Antonio Novais, 12. Ciudad Universitaria, 28040, Madrid, Spain

13 ³Departamento de Geología, Universidad de Salamanca, Pza. de los Caídos s/n, 37008, Salamanca, Spain

14 ⁴Department of Earth Science, University of California, Santa Barbara, CA 93106, United States

15 ⁵Earth Science Department, Durham University, Science Labs, Durham DH1 3LE, United Kingdom

16

17

18 Correspondence to: J. Gómez Barreiro (jusb@usal.es)

19

20 jose.benitez@ctn.tecnico.ulisboa.pt

21 castigar@ucm.es

22 jrmc@usal.es

23 kylander@geol.ucsb.edu

24 r.e.holdsworth@durham.ac.uk

25

26 **Abstract**

27 The Sobrado unit, within the upper part of the Órdenes complex (NW Iberia) represents an
28 allochthonous tectonic slice of exhumed high grade metamorphic rocks formed during a complex
29 sequence of orogenic processes in the middle to lower crust. In order to constrain those processes, U-Pb
30 geochronology and REE analyses of accessory minerals in migmatitic paragneisses (monazite, zircon),
31 and mylonitic amphibolites (titanite) were conducted using LASS-ICP-MS. The youngest metamorphic
32 zircon age obtained coincides with a Middle Devonian concordia monazite age (~380 Ma) and is
33 interpreted to represent the minimum age of the Sobrado high-P granulite-facies metamorphism that
34 occurred during the early stages of the Variscan Orogeny. Metamorphic titanites from the mylonitic
35 amphibolites yield a Late Devonian age (~365 Ma) and track the progressive exhumation of the Sobrado
36 unit. In zircon, cathodoluminescence images and REE analyses allow two aliquots with different origins
37 in the paragneiss to be distinguished. An Early Ordovician age (~490 Ma) was obtained for metamorphic
38 zircons, although with a large dispersion, related to the evolution of the rock. This age is considered to
39 mark the onset of granulite-facies metamorphism in the Sobrado unit under intermediate-P conditions,
40 and related to intrusive magmatism and coeval burial in a magmatic arc setting. A maximum depositional
41 age for the Sobrado unit is established in the late Cambrian (~511 Ma). The zircon dataset also record
42 several inherited populations. The youngest cogenetic set of zircons yields crystallization ages of 546 and
43 526 Ma and are thought to be related to the peri-Gondwana magmatic arc. The additional presence of
44 inherited zircons older than 1000 Ma is interpreted as suggesting a West African Craton provenance.

45 **Keywords:** U-Pb geochronology, LASS-ICP, zircon, titanite, monazite, REE, Sobrado Unit

46

47

1 **1. Introduction**

2 Zircon, monazite and titanite are accessory mineral phases found in rocks with a very wide range
3 of compositions. These minerals can resist numerous sedimentary, igneous and metamorphic events
4 across a wide range of temperatures, pressures and strains, even when fluids are present. Frequently,
5 compositional domains can be defined in these minerals that record changes in different parameters
6 (Storey et al., 2007; Castiñeiras et al., 2010; Stübner et al., 2014; Hacker et al., 2015; Stearns et al., 2016;
7 Stipska et al., 2016). These minerals additionally provide several closed decay chains or disintegration
8 systems ($^{238}\text{U} \rightarrow ^{206}\text{Pb}$, $^{235}\text{U} \rightarrow ^{207}\text{Pb}$ y $^{232}\text{Th} \rightarrow ^{208}\text{Pb}$), because they hold variable concentrations of
9 uranium (U) and/or thorium (Th) in their crystal lattices. Such variations in concentration allow accurate
10 dating using microscopic scale analysis (tens of microns size).

11 Titanite is stable in metabasites across a wide range of metamorphic conditions (Spear, 1981;
12 Frost et al., 2000) and is able to record metamorphic and deformational events (Franz and Spear, 1985;
13 Verts and Frost, 1996; Rubatto and Hermann, 2001; Spencer et al., 2013; Stearns et al., 2015, 2016). The
14 titanite U/Pb system is a widely used geochronometer for deformation events in granulite-amphibolite
15 facies rocks (Spear, 1981; Cherniak, 2006; Harlov et al., 2006). Monazite is common in amphibolite and
16 higher-grade facies. Zoning in this mineral can have an igneous or metamorphic origin (DeWolf et al.,
17 1993; Hawkins and Bowring, 1997; Zhu et al., 1997; Spear and Pyle, 2002). The crystallization stages
18 seen in zoned monazites, with changes in Y, Ca, Si, Sr, Ba, REE, U and Th, has been linked to certain
19 metamorphic reactions (Kohn and Malloy, 2004; Corrie and Kohn, 2008) or deformation process (Terry
20 and Hamilton, 2000). Zircon survives the majority of magmatic, metamorphic and erosive terrestrial
21 processes. Cathodoluminescence analysis of zircon zoning patterns allows a large variety of reactions to
22 be distinguished and can clarify the petrogenetic evolution (Corfu et al., 2003). Th/U ratios can also be
23 used to separate zircon based on their igneous or metamorphic origin (Hoskin and Ireland, 2000; Möller
24 et al., 2002; Hokada and Harley, 2004; Hoskin, 2005). Rare-earth element (REE) abundances can also be
25 used as a qualitative petrological indicator. Heavy rare-earth elements (HREE) are preferentially
26 incorporated into zircon compared to light rare-earth elements (LREE). Hence, the normalized HREE
27 slope can be used to interpret whether a zircon crystallized or recrystallized when garnet and xenotime
28 (YPO_4) were present, because these minerals also preferentially assimilate HREE in the lattice (Hoskin
29 and Ireland, 2000; Rubatto, 2002; Hermann and Rubatto, 2003; Rubatto et al., 2009).

30 The events recorded in individual grains can be radiometrically dated employing combined laser
31 ablation analyses and cathodoluminescence (CL) images in zircons (Corfu et al., 2003) and compositional
32 maps obtained using electron microprobe (EMPA) in monazite (Gonçalves et al., 2005; Williams et al.,
33 2007) to recognize different growth zones. The chemical analysis, especially REE, links the development
34 of growth zones to specific metamorphic or deformative events (Frost et al., 2000; Rubatto, 2002;
35 Whitehouse and Platt, 2003; Zheng et al., 2007; Chen et al., 2010; Gagnepain and Daly, 2010; Holder et
36 al., 2015;). Simultaneous geochronology and REE data are a powerful tool in the interpretation of ages -
37 this is known as REE-assisted geochronology (Castiñeiras et al., 2010).

38 This methodology has been applied to selected samples of the Sobrado unit (Fig. 1), which forms
39 part of the allochthonous complexes of NW Iberia and one where the structural and metamorphic
40 evolution is rather well known (Pablo Maciá et al., 1984; Díaz García et al., 1999; Arenas and Martínez
41 Catalán, 2002; Benítez-Pérez, 2017). This unit occurs in the Upper Allochthon of the Órdenes complex,
42 and represents a tectonic slice of exhumed ultramafics, eclogites, high-P granulites, amphibolites and
43 migmatitic paragneisses derived from a peri-Gondwanan terrane. It evolved along a complex sequence of
44 geological processes involving Cambro-Ordovician rifting with voluminous bimodal plutonism, nearly
45 contemporaneous granulite facies metamorphism of intermediate-P, early Variscan subduction and
46 subsequent exhumation by ductile thrusting during Variscan collision with the external margin of
47 northern Gondwana.

1 Previous geochronological data on the Sobrado unit include U-Pb ages from four samples
2 (Fernández-Suárez et al., 2002, 2007). A middle Cambrian protolith age of a gabbro and a Middle
3 Devonian metamorphic age of a high-P basic granulite supposedly derived from the same gabbro were
4 obtained by zircon dating. Zircon in a migmatitic, mylonitized paragneisses yielded discordant ages with
5 an Early Ordovician lower intercept, while monazite dating provided Cambro-Ordovician ages in another
6 migmatitic, mylonitized paragneiss. This new study aims at constraining the metamorphic evolution of
7 the unit including dating a migmatitic paragneiss, as previous data missed the early Variscan ages found
8 in intercalated high-P granulites, and also an amphibolite, which could date advanced stages of
9 exhumation. Monazite and zircon ages of paragneisses and titanite ages of amphibolites taken from
10 separate, but presently adjacent tectonic slices of the high-P/high-T of Sobrado unit are compared and
11 interpreted using REE-assisted geochronology. This sheds new light upon the possible origin, ages and
12 relationships between the regional foliation development and the partial melting processes that have
13 occurred in this and equivalent units of the NW Iberia Upper Allochthon.

14

15 2. Geological background

16 The Allochthonous complexes in NW Iberia are remnants of a huge nappe stack preserved as
17 klippen in the core of late Variscan synforms. They consist of units mostly of peri-Gondwanan derivation,
18 which can be classified in three groups based on their structural position in the tectonic pile and origin:
19 The Upper, Middle and Lower allochthons (Fig. 1).

20 The Upper Allochthon is a piece of the northern margin of Gondwana detached and drifted away
21 during the Cambro-Ordovician opening of the Rheic Ocean. The Middle Allochthon is formed by
22 lithospheric pieces of oceanic affinity, or oceanic supracrustal sequences that formed part of the Rheic
23 oceanic realm and are often referred to as ophiolitic units. The Lower Allochthon derives from distal parts
24 of the Gondwanan continental margin.

25 The Allochthon units are separated from the Iberian Autochthon by a series of kilometer-scale
26 imbricated sheets, known as the Parautochthon (Ribeiro et al., 1990), or Schistose Domain in Galicia
27 (NW Spain), consisting of a set of Paleozoic metasedimentary and volcanic rocks. The Parautochthon has
28 stratigraphic and igneous affinities with the Iberian autochthon of the Central Iberian Zone, and no
29 ophiolites occur between them. For these reasons it is interpreted as a distal part of the Gondwanan
30 continental margin (Farias et al., 1987; Dias da Silva et al., 2014).

31 The allochthonous units are regarded as a stack of Varican thrust sheets with associated tectonic
32 fabrics and metamorphic events. Due to the "piggy-back" nature of the sequence, the structurally higher
33 units are thought to represent the furthest travelled paleogeographic domains. Recumbent folds, thrusts
34 and extensional detachments formed during the Variscan collision are found in all three allochthonous
35 units (Martínez Catalán et al., 1999; Gómez-Barreiro et al., 2007).

36 Maximum sedimentation ages obtained from the study of detrital zircon carried out in
37 metasediments from the Upper allochthon can be estimated between 530 and 510 Ma (e.g., Fuenlabrada
38 et al., 2010). Intrusive rocks in the Upper allochthon have been dated between 520 and 490 Ma and are
39 associated with the development of a magmatic arc which evolves into an extensional scenario that ended
40 with the opening of the Rheic ocean (Peucat et al., 1990; Ordóñez Casado, 1998; Abati et al., 1999, 2007;
41 Fernández-Suárez et al., 2007; Castiñeiras et al., 2010). Two high-P/high-T metamorphic events have
42 been recognized in this unit. The oldest one has yielded 490-480 Ma (Kuijper 1979; Peucat et al. 1990;
43 Abati et al., 1999, 2007; Fernández-Suárez et al., 2002) and the youngest one has been dated
44 approximately between 405-390 Ma (Santos Zalduegui et al., 1996; Ordóñez Casado et al., 2001;
45 Fernández-Suárez et al., 2007). In the Middle allochthon, crystallization ages vary between 390 and 375
46 Ma (Peucat et al., 1990; Dallmeyer et al., 1991, 1997) and ages from 375 to 365 Ma have been related to
47 continental subduction (Santos Zalduegui et al., 1995; Abati et al., 2010). Thrust wedge collapse, in the

1 middle and lower allochthonous units, is thought to have happened between 390 and 365 Ma, followed by
2 a collision in the internal zones around 365-330 Ma, causing further folding and thrusts (Dallmeyer et al.,
3 1997; Martínez Catalán et al., 2009). Afterwards, there was another extensional collapse phase until 315
4 Ma, followed by a final phase of shortening and folding up until approximately 305 Ma related to the
5 regional orocinal bending in Iberia (Aerden, 2004; Martínez Catalán, 2011, 2012; Álvarez-Valero et al.,
6 2014).

7 The Upper Allochthon is further subdivided into high-P/high-T and intermediate-P units (Gómez
8 Barreiro et al., 2007). The present study focuses on two of the high-P/high T upper units (Figs. 1 and 2).
9 The origin of the high-P event recorded in these units is controversial, but might reflect the accretion of
10 the units into the continental part of northern Gondwana, during the Early-Middle Devonian (400-390
11 Ma; Ballèvre et al., 2014).

12

13 The Sobrado antiform consists of three tectonic slices or horses bounded by two extensional
14 detachments (Figs. 1 and 2). The lower horse comprises highly serpentinized ultramafic rocks with
15 interlayered metabasite units. The metabasites include eclogites ($Omp + Grt + Qtz + Rt \pm Ky$ and Zo ,
16 mineral abbreviations according Whitney and Evans, 2010) and related clinopyroxene-garnet rocks
17 without primary plagioclase ($Na-Di + Grt + Qtz + Rt \pm Zo$), as well as other types of rocks derived from
18 the retrogression and mylonitization of the early high-P stages. The intermediate horse is made up of
19 migmatitic felsic gneisses (mainly paragneisses), with frequent inclusions of high-P granulites ($Na-Di +$
20 $Grt + Pl + Qtz + Rt \pm Ky$). Remnants of igneous protoliths are not preserved either in the lower or
21 intermediate horses. The upper horse, however, contains migmatitic felsic gneisses and mafic layers
22 derived from deformed and recrystallized gabbros with locally preserved relict igneous textures, reaching
23 high-P granulite facies conditions. The progressive transformation gabbros to high-P granulites ($Na-$
24 $Di + Grt + Pl + Qtz + Rt$) has occurred in a series of different stages with a metamorphic peak at 13-17
25 kbar and 660-770°C (Arenas and Martínez Catalán, 2002).

26 The metamorphic evolution described by most authors in the Sobrado Unit suggests that felsic
27 gneisses underwent differing degrees of partial melting after the metabasites reached their peak pressure.
28 Consequently, the felsic gneisses are thought to have developed a regional foliation under amphibolite
29 facies conditions, as did the amphibolic gneisses, "flaser" amphibolites, and fine-grained amphibolites.
30 This metamorphic evolution is described by Arenas and Martínez Catalán (2002) as a clockwise P-T path,
31 with a metamorphic peak of, at least, 15 kbar and >800°C, followed by a strongly isothermal and
32 decompressive trajectory. This trajectory is interpreted to result from gravitational collapse of an
33 overthickened orogenic wedge (Gómez-Barreiro et al., 2007; Ballèvre et al., 2014). Although some
34 regional structures, such as the Fornás detachment (FD, Fig. 1; Gómez-Barreiro et al., 2007; Álvarez-
35 Valero et al., 2014) or the Corredoiras detachment (CD, Fig. 1; Díaz García et al., 1999), have been
36 related to this gravitational readjustment, no study has dealt with the development of the extensional
37 fabrics in any detail. Overall, it is thought that the extensional flow has generated a pervasive thinning of
38 the orogenic pile and that the preserved sequence of tectonic slices is strongly condensed.

39 3. Sample description and Methodology

40 3.1. Selected samples

41 Two representative samples (*JBP-71-15A* and *JBP-71-21*) were selected from two structurally
42 separate but currently adjacent parts of the high-P/high-T Sobrado unit, within the Órdenes complex, for
43 laser ablation (LASS-Laser Ablation Split Stream) analyses, including U-Pb geochronology and REE
44 determinations. The samples locations are presented in Figure 2.

45 Sample *JBP-71-21* is a mylonitic fine-grained amphibolite, without any preserved igneous
46 relicts. Fine-grained amphibolites represent an advanced stage in the mylonitization of the metabasites.
47 They appear as relatively thin layers inside the mafic rocks and dominate in a thick mylonitic layer (300

1 - 700m; Fig. 2; Arenas and Martínez Catalán, 2002; Benítez Pérez, 2017) located at the base of the upper
2 tectonic horse. The sample comprises Hbl + Pl + Grt ± Cpx + Bt ± Rt ± Ttn ± Ilm ± Zo ± Qtz (Fig. 3).
3 Mylonitic foliation and lineation are defined by amphibole and plagioclase (Fig. 3). Garnet appears as
4 subrounded porphyroclasts partially resorbed (Fig. 3). Titanite grains are parallel to the foliation and in
5 textural equilibrium with plagioclase and amphibole. Single crystal titanite fish (Passchier and Trouw,
6 2005) are coherent with the kinematic of the shear zone (Ttn-fish; Fig. 3 e). Rutile and ilmenite are
7 always included both in titanite and/or garnet (Fig. 3 c, d and f).

8 Sample *JBP-71-15A* is a granulite facies migmatitic paragneiss from the underlying intermediate
9 tectonic horse. It comprises Qtz + Pl + Grt + Kfs + Ky + Bt + Ilm + Rt and shows microscopic scale
10 textural evidence of partial melting. Temperature and pressure estimation ranges between 750-850°C and
11 11-16 kbar for the anatetic fabric (Benítez-Pérez, 2017). Leucocratic domains with Qtz, Kfs and Pl, with
12 evidence of plastic deformation define the foliation and Bt, Ky, Rt and Grt define linear aggregates
13 resulting in a pervasive lineation (Fig. 4). Along the strained leucosomes, garnets show evidence of
14 plastic deformation (Benítez Pérez, 2017) like (Fig. 4 a, f, g): sigmoidal, dumb-bell-shaped grains and
15 pinch-and-swell microstructures (Ji and Martignole, 1994; Kleinschrot and Duyster, 2002; Passchier and
16 Trouw, 2005). Zircon and monazite are found in different microtextural settings. Small-elongated prisms
17 of zircon are always found shielded within garnets (Fig. 4 g), while relatively larger zircon grains with
18 irregular, elongated, sub-rounded shapes, appear across the fabric in leucosomes, biotite aggregates and
19 even within kyanite crystals (Fig. 4 a,b,c,d,f). In few cases, elongated/sub-rounded zircons have been
20 found as inclusions in garnets (Fig. 4 e). Monazite grains show elongated to sub-rounded grains located in
21 Qtz-Kfs-Pl-Bt domains, which define the main foliation of the rock (Fig. 4 d,f,h).

22 3.2. Sample preparation

23 Sample preparation was carried out at the laboratories of the Universidad Complutense (Madrid).
24 The rocks were crushed, pulverized and sieved to achieve a 0.1-0.5 mm grain size. Heavy minerals were
25 concentrated using a Wilfley™ table. The non-magnetic minerals from this heavy fraction are then
26 separated using a Frantz isodynamic magnetic separator. A final concentrated fraction is obtained using
27 heavy liquids (methylene iodide, CH₂I₂).

28 Zircon (translucent, colourless or light brown), monazite (yellow) and titanite (colorless) grains
29 are selected by handpicking, according to their external morphology viewed under a binocular
30 microscope. All the grains collected were arranged separately in parallel rows, mounted on glass slide
31 with a double-sided adhesive and set in epoxy resin. After the resin was cured, the surface was eroded
32 using a wet abrasive silicon carbide abrasive paper (4000 grit) and polished with 0.3 µm aluminium
33 oxide. The surface was then coated with gold, to avoid charging problems under the scanning electron
34 microscope (SEM). Prior to isotopic analysis, cathodoluminescence images (CL) of zircon grains were
35 taken on a JEOL JSM-820 SEM, and compositional maps of monazite grains were created on a JEOL
36 Superprobe JXA-8900M microprobe (National Center for Electron Microscopy, Madrid). Secondary
37 electron images (SE) were also taken to determine the exact location of the spots, identify the internal
38 structure, and presence of inclusions and defects in zircon, monazite and titanite grains.

39

40 3.3. Mineral description

41 Titanite grains are generally rounded, with an average grain size of 100 µm, and irregular
42 morphologies. Their secondary electron images reveal homogeneous compositions and the presence of
43 solid inclusions. This grain size permits large spatial resolution analyses (50 µm) to be carried out.
44 Monazite grains have a more variable grain size distribution, with an average of 60-70 µm. Their habit is
45 irregular and they usually show rounded morphologies or broken grains. We carried out La, Th, Y, U and
46 Nd compositional maps for every monazite grain in order to discover a compositional zonation that could
47 be attributed to different growth events. Thorium zoning is the one that developed better and was taken

1 into account to select the spots for isotopic analysis (Fig. 5), yet it never exceeds 30% of the grain.
2 Several spots were analyzed in monazite crystals with the greatest compositional contrasts to determine if
3 they really represented different growth stages in the monazite grains.

4

5 Zircon grains from the paragneisses usually have scarce mineral inclusions and they can display
6 a wide variety of morphologies, including irregular and sub-rounded shapes typical of metamorphic
7 zircon, pristine elongated dipyratidal prisms interpreted as igneous in origin, and equigranular grains
8 with abrasion signs with a probable detrital origin. Their length-to-width ratios vary between 3:1 and 2:1.
9 Cathodoluminescence images (Fig. 6) are useful to relate the crystallization of parts of zircon crystals to
10 specific igneous, metamorphic or deformational events (Corfu et al., 2003, Nasdala et al., 2003, Zeck et
11 al., 2004). It is common to image a homogeneous xenocrystic core in zircon grains and even a less
12 luminescent mantle in some grains (grain numbers 5, 6). The core aspect is mainly rounded, with
13 irregular or angular shapes. In most of the zircon grains, the internal parts of the grains display an
14 oscillatory zoning (grain numbers 33, 71), with different thickness, although in some cases, this zoning is
15 faint (grain number 26). There are several grains with sector zones (grain numbers 26, 27) parallel to the
16 zircon *c*-axis (Watson and Yan Liang, 1995) and even one case of soccerball zoning (grain number 82).
17 The zoning usually appears to be partially truncated and surrounded by a discontinuous poorly
18 luminescent rim (grain numbers 20, 79).

19

20 3.4. Analytical techniques

21 U/Th-Pb, REE and Hf analyses of zircon, titanite and monazite were carried out using the laser
22 ablation split stream (LASS) at the University of California at Santa Barbara (UCSB). The samples were
23 ablated using a Photon Machines 193 nm ArF excimer ultraviolet laser with a HelEx ablation cell coupled
24 to a Nu Instruments Plasma high-resolution multi-collector inductively coupled plasma mass
25 spectrometer (MC-ICP-MS) and either a Nu Instruments AttoM high-resolution single-collector ICP or
26 an Agilent 7700S quadrupole ICP-MS (Kylander-Clark et al., 2013). This installation allows the
27 simultaneous isotopic and compositional (REE) analysis to be carried out. The laser spot diameter was 20
28 μm for zircon, 7-10 μm for monazite (Košler et al., 2001) and 50 μm for titanite (Stearns et al., 2016),
29 resulting in pit depths between 6 μm for monazite and 30 μm for titanite. The laser has a fluence of ~ 1
30 J/cm^2 and was fired twice to remove common Pb from the sample surface. This material was allowed to
31 wash out for 15 s, prior to the material being ablated at 3 Hz for 20 s for analysis. On the ICP-MS, the
32 masses $^{204}\text{Pb}+\text{Hg}$, ^{206}Pb , ^{207}Pb , and ^{208}Pb were measured using ion counters, and the masses ^{232}Th and
33 ^{238}U were measured using Faraday detectors.

34 The U/Th-Pb standardization for monazite was carried out using sample 44069 (Aleinikoff et al.,
35 2006) as the primary reference material (RM), whereas the Bananeira sample was employed as primary
36 RM for trace element corrections (Kylander-Clark et al., 2013; Palin et al., 2013). Additionally, FC-1
37 (Horstwood et al., 2003), Trebilcock (Tomasca et al., 1996) and Bananeira were also used as secondary
38 monazite RM, allowing $^{206}\text{Pb}/^{238}\text{U}$ ages to be within 2% of their accepted values. U-Pb proportions in
39 titanite were corrected using Bear Laken (Aleinikoff et al., 2007) and Y1710C5 (Spencer et al., 2013) as
40 RM. 91500 (Wiedenbeck et al., 1995) and GJI (Jackson et al., 2004) were used as RM for zircon, both
41 for isotopic composition and trace element calibrations. Radiogenic lead versus common lead
42 ($^{207}\text{Pb}/^{206}\text{Pb}$) measurements require up to 2% additional external error attributable either to variation count
43 statistics, or ablation signal stability (Spencer et al., 2013; Hacker et al., 2015b). These external errors
44 were incorporated into the data in the experiments.

45 The Iolite plug-in v. 2.5 (Paton et al., 2011) from the Wavemetrics Igor Pro software was used to
46 improve and reduce the analyses (Hacker et al., 2015). The isotopic ratios $^{238}\text{U}/^{206}\text{Pb}$ and $^{207}\text{Pb}/^{206}\text{Pb}$ for
47 each analysis were plotted on Tera-Wasserburg diagrams using Isoplot and Topsoil programs (Ludwig,

1 2012; Zeringue et al., 2014). All date uncertainties are reported at the 95% confidence interval, assuming
2 a Gaussian distribution of measurement errors. Zircon, titanite, and monazite REE analyses were
3 normalized against the McDonough and Sun (1995) chondrite values.

4 **4. Results**

5 **4.1. Titanite (amphibolite, upper horse)**

6 Fifty-one titanite analyses were projected onto a Tera-Wasserburg concordia plot (Fig. 7 a).
7 After a preliminary evaluation, twelve analyses were rejected due to either high common Pb or high
8 discordance ($>10\%$) and were considered no further (Table 1). The remaining analyses define a Pb/U
9 semi-total isochron between the common or initial Pb (^{207}Pb) and radiogenic Pb (^{206}Pb) (Ludwig, 1998).
10 The good fit of the isochron confirms the chemical homogeneity of the data (Stearns et al., 2016) and it
11 intercepts the concordia at 364.8 ± 4.5 Ma (2σ). Titanite chondrite-normalized REE analyses are detailed
12 in Table 1 and are shown in Fig. 7 b. Titanite REE patterns are convex upwards, relatively flat, with slight
13 LREE depletions versus HREE with respect to chondrite. They generally lack a europium anomaly (Eu*),
14 but some analyses show a non-distinctive positive or negative anomaly.

15 **4.2. Monazite (paragneiss, middle horse)**

16 For monazite U/Th-Pb geochronology, we used the thorium zoning in monazite grains to select
17 the analytic spots. As shown in Figure 5 there are no significant age differences between spots or zones
18 with different Th chemical concentrations in a single grain. The obtained REE patterns are also very
19 similar, and the mismatch at the HREE is probably due to either uncertainties in measurement because of
20 the lower counts or interference effects of intermediate rare-earth oxides (Holder et al., 2015).

21 Data from seventy-six U/Th-Pb monazite analyses are shown in Table 2 and displayed using a
22 Tera-Wasserburg concordia plot (Fig. 8 a). Four of these analyses, not related to chemical zoning, were
23 discarded due to common Pb loss and were considered no further. The remaining analyses form a single
24 population (mean square of weighted deviation; MSWD = 0.48) centered on a concordia age of $382.5 \pm$
25 1.0 Ma (2σ). Monazite geochemistry is shown in Figure 8b. REE patterns analyzed show an LREE
26 enrichment, HREE depletion and negative Y anomalies with respect to chondrite with little variation
27 within or between samples.

28 **4.3. U-Pb zircon (paragneiss, middle horse)**

29 Eighty-three analyses were performed on eighty zircon grains from the Sobrado paragneiss
30 (Table 3). In a preliminary assessment of the data two analyses were rejected due to analytical errors
31 (grain numbers 8, 36). Additionally, 23 analyses yielded a discordance higher than 10% and will not be
32 further considered. The remaining 58 zircon analyses are shown on a Wetherill concordia plot (Fig. 9 a).
33 The $^{207}\text{Pb}/^{206}\text{Pb}$ ages older than 1000 Ma are presented in a probability density plot (Fig. 9b). Most of the
34 old ages are distributed between 1880 and 2200 Ma, with two peaks at 2030 and 2100 Ma. Three ages are
35 older, around 2600 Ma, and there are also two analyses around 1300 Ma. The $^{206}\text{Pb}/^{238}\text{U}$ ages younger
36 than 1000 Ma are plotted in a Tera-Wasserburg concordia plot (Fig. 10 a) and a probability density plot
37 (Fig. 10 b). The data are continuously distributed between 589 and 380 Ma and attending to their CL
38 texture, ages from 589 to 510 Ma are obtained mainly from internal areas with oscillatory or sector
39 zoning (e.g., 33, 27 and 62, see Fig. 6); whereas, ages from 510 to 380 Ma correspond to discordant rims
40 that have homogeneous CL signal, except for some grains (e.g., 10, 11 and 26, see Fig. 6) that are cores
41 with oscillatory or sector zoning.

42 **4.4. REE zircon (paragneiss, middle horse)**

43 The chondrite-normalized REE patterns of the zircons with ages older than 600 Ma are shown in
44 Figure 11. In general, this group has REE patterns with a pronounced fractionation from light to heavy
45 REE and two anomalies in Ce (positive) and in Eu (negative). There are only three analyses that diverge
46 from this template and show a flat HREE pattern.

For the younger analyses, the chondrite-normalized REE patterns have different features depending on the age (Fig. 12). The oldest ages (589–510 Ma) show a tight HREE fractionation, variable Eu anomaly, and a pronounced Ce anomaly. The youngest ages (510–380 Ma) has a variable HREE slope, whereas the Eu anomaly is more regular, and the Ce anomaly is less marked.

When we plot age versus Hf, Yb/Gd and Eu/Ey* (Figs. 13 a, b, c), the group of oldest ages (589–510 Ma) do not define any apparent trend. In sharp contrast, in the 500–380 Ma group it is remarkable not only the good correlation between age and composition, but also the divergent evolution depending of the age (grey arrows). Hafnium, Yb/Gd and Eu/Ey* increase from 500 to ~430 Ma while there is a striking decrease from ~420 to 380 Ma. Finally, we have used the U/Ce-Th graph proposed by Bacon et al. (2012) to discriminate between metamorphic and igneous zircon. In this diagram, the first group of zircon plot in the igneous field, whereas the second group of zircon is projected in the metamorphic field (Fig. 13 d).

5. Discussion

5.1. Zircon inheritance

The presence of zircon grains shielded by garnets (e.g. Fig. 4 e and g) is compatible with the preservation of magmatic, metamorphic or detrital inheritances during the synkinematic partial melting recorded in these rocks (Benítez Pérez, 2017). As shown in Fig 12, the majority of analyzed zircon grains older than 600 Ma have fractionated REE patterns that are characteristic of igneous zircon (Hoskin and Schaltegger, 2003; Whitehouse and Platt, 2003; Hanchar and Westrenen, 2007; Grimes et al., 2015). Only three analyses show a flat HREE pattern that can be related to the presence of garnet and interpreted as metamorphic zircon. The provenance of the zircon grains older than 600 Ma in the Sobrado migmatitic paragneisses (Fig. 9 b) has close affinities to the results obtained in other U-Pb geochronology studies of detrital zircons and Sm-Nd whole rock analyses in intermediate-P units of NW Iberia upper allochthons (Betanzos unit, Fuenlabrada et al., 2010; Cariño gneisses, Albert et al., 2015). We obtained two Mesoproterozoic ages, between 1.2 and 1.4 Ga. Similar ages are also found in the Parautochthonous (Díez Fernández et al., 2012), in the basal allochthonous units (Díez Fernández et al., 2010) and, to a lesser extent, in the intermediate-P units of NW Iberia (Albert et al., 2015). These inherited zircons, although scarce (Fernández-Suárez et al., 2003), likely have their origin in rocks derived from Saharan and Arabian-Nubian cratons, and presumably transported during the Cadomian orogeny (e.g., Martínez Catalán et al., 2004). Paleoproterozoic populations range from 1.8 to 2.2 Ga, clustered at 2.1 Ga, are also common in the Allochthonous complexes (Fernández-Suárez et al., 2003) and their origin likely involves materials generated or reworked during the Eburnian orogeny (e.g., Egal et al., 2002; Ennih and Liegeois, 2008) from the West African craton (Peucat et al., 2005). Finally, the Archean population in the Sobrado paragneisses ranges from 2.5 to 2.8 Ga, and it is likely related to intrusive events in the Western Reguibat Shield (Schofield et al., 2012) and the northern part of the West African craton (Albert et al., 2015), with some reworking processes of juvenile rocks formed at ca. 3.0 Ga (Potrel et al., 1998).

Based on CL images, ages and zircon composition, we can determine that the youngest zircon with magmatic origin is grain number 34 (Fig. 6). The number obtained in this grain is comparable to other maximum depositional ages obtained from similar units in the NW Iberia allochthonous complexes, such as the intermediate-P Betanzos uppermost unit (530–510 Ma, Fuenlabrada et al., 2010), and the intermediate-P Cariño uppermost unit (~510 Ma, Albert et al., 2015).

In order to get more insight into the meaning of the data younger than 600 Ma, we have plotted these ages versus the Th/U ratios (Fig. 14). Analyses that yielded ages between 589 and 510 Ma cluster together with Th/U values higher than 0.3. The REE patterns displayed in this cluster are consistent with a magmatic origin. In the age versus Hf, Yb/Gd and Eu/Ey* plots for this group (Fig. 13 a, b, c), the absence of a trend suggests that the different zircon grains are not connected by a fractional crystallization process (e.g., Barth and Wooden, 2010). In the U/Ce-Th graph proposed by Bacon et al. (2012) to discriminate between metamorphic and igneous zircon. In this diagram, zircon with ages between 589 and 510 Ma plot in the igneous zircon field (Fig. 13 d).

1 From the first group of data between 589 and 510 Ma, we can extract two ages, 546 ± 5 Ma out
2 of six analyses, and 526 ± 3 Ma from 14 analyses (Fig. 15). These magmatic ages are also recognized in
3 other well-characterized high-P/high-T units of the allochthonous complexes (Peucat et al., 1990; Santos
4 Zalduegui et al., 2002; Castiñeiras et al., 2010), and they are related to a magmatic arc creation around the
5 periphery of Gondwana (Abati et al., 1999, 2007).

6

7 **5.2. Evolution of metamorphism of the Sobraço migmatitic paragneiss based on zircon 8 composition**

9 Extracting ages from a dataset where the data are evenly distributed from 500 to 380 Ma is a
10 challenging task. When such smear in the age sorting happens, if we can rule out analytical error, we have
11 three possibilities (e.g., Castiñeiras et al., 2010), namely, (i) the correct age is the youngest and the
12 dispersion is related to zircon inheritance, (ii) the real age is the oldest and the spread is caused by lead
13 loss, or, (iii) the age range is recording some kind of protracted geological event. Taking into account the
14 CL texture of the youngest spots, we can remove the first possibility as the majority of analyses were
15 performed in zircon rims. Furthermore, maximum depositional ages obtained from similar units from the
16 Allochthonous complexes preclude their interpretation as inheritance. The second possibility is plausible,
17 considering the complex metamorphic evolution and the high grade attained by these rocks. However, a
18 young lead loss episode should have affected also the inherited zircon ages, and the presence of various
19 old age peaks (e.g., ~2000, 546 and 536 Ma) suggests that they did not experienced lead loss. However,
20 we can argue that limited lead loss occurred in some grains that have similar composition to the 589-510
21 Ma group ($\text{Th/U} > 0.15$), but younger ages (between 502 and 468 Ma). This group of outlier analyses
22 (#10, 11, 26 and 63) could have experienced a decoupling between their actual age and their composition
23 (e.g., Flowers et al., 2012). Finally, we favor the last option when we take into account the strong
24 correlation observed between age and zircon composition (Figs. 13 a, b, c and 14).

25 This group of young analyses defines a trend with negative correlation from 500 to 380 Ma and
26 Th/U values from 0.01 to 0.13. This correlation between the age and the composition of zircon suggests
27 that the age dispersion is related to an actual geological process and is not caused by lead loss.
28 Furthermore, even though the Th/U ratio shows a consistent evolution from 510 to 380 Ma, the rest of the
29 proxies considered (Hf, Yb/Gd and Eu/Eu*, Figs. 13 a, b, c) point out to a two-stage evolution, and the
30 characteristics of the REE patterns are compatible with a metamorphic origin (Chen et al., 2009, 2010;
31 Rubatto et al., 2009; Peters et al., 2013; Stipska et al., 2016).

32 This is congruent with the presence of two metamorphic events in the HP-HT units, one at 490-
33 480 Ma and other at ~390-380 Ma (e.g., Fernández-Súarez et al., 2002, 2007). The increase recorded in
34 Yb/Gd (Fig. 13 b), related to the slope of the HREE, from 502 to 430 Ma is congruent with a higher
35 availability of HREE in the rock. As garnet is the most important HREE reservoir in metamorphic rocks,
36 we argue that this trend is recording the progressive destabilization of garnet in a decompressive path
37 from HP-HT conditions. The increase observed in the Eu/Eu* ratio is consistent with a progressive
38 retrogression of anorthite, which is the main europium reservoir in rocks (Barth and Wooden, 2010;
39 Castiñeiras et al., 2011).

40 The sharp decrease observed in the Yb/Gd ratio from 420 to 380 Ma, is probably related to a
41 new event of garnet growth (Rubatto et al., 2006; Stipska et al., 2016), i.e., the second HP-HT event. The
42 evolution in the Eu/Eu* ratio suggests that this event took place under granulite facies conditions, as
43 plagioclase was present to pump out all the available europium.

44

45 **5.3. Age of the youngest metamorphism in the Sobraço antiform**

46 The youngest zircon data recorded (380 ± 4 Ma) is coherent with the monazite concordia age
47 (382 ± 1 Ma) in the migmatitic paragneisses of the Middle tectonic horse. Besides, both monazite and
irregular/sub-round zircons share their microtextural setting along the migmatitic fabric, pointing to a

1 coeval character with partial melting at relatively high-P. Furthermore, the chemical profiles observed in
2 the monazite suggest simultaneous crystallization of this mineral with garnet (Rubatto, 2002; Rubatto et
3 al., 2006; Mottram et al., 2014; Holder et al., 2015), which is stable at paleogeresses typical temperatures
4 and pressures. Negative Eu anomalies indicate a preferential incorporation of europium to feldspars, in
5 particular to K-feldspar, during melt crystallization (Buick et al., 2010; Rubatto et al., 2013). These
6 characteristics are compatible with monazite crystallization in a single pulse ($\text{MSWD} < 1$) in the presence
7 of garnet, supporting its metamorphic origin. This Middle Devonian age can be interpreted to represent
8 the *minimum* age of the youngest metamorphic event in Sobrado unit, which reached high-P granulite
9 facies (Fernández-Suárez et al., 2007; Ordóñez Casado et al., 2001). It is suggested that monazite captures
10 the onset of the exhumation process in the migmatitic paragneisses (Holder et al., 2015). Titanite
11 crystallization is synkinematic with the mylonitic fabric of the fine-grained amphibolites located at the
12 base of the Upper tectonic horse. The growth of titanite in amphibolitic conditions is supported by the
13 umbrella-shaped REE patterns shown in Fig. 7b, typical of titanite coexisting with amphibole (Mulrooney
14 and Rivers, 2005; Chambefort et al., 2013; Lesnov, 2013). A Late Devonian age (~365 Ma) could be
15 related to the onset of retrograde metamorphic conditions during the development of the shear zone, and
16 suggests a protracted exhumation process, reaching amphibolite facies. The Late Devonian age lies
17 close to the Ar/Ar exhumation ages of the uppermost units in the Órdenes complex as recorded in the
18 Corredoiras detachment (376 ± 2.0 Ma in hornblende, Dallmeyer et al., 1997), or in the Ponte Carreira
19 Detachment (371 ± 4.0 Ma in muscovite, Gómez Barreiro et al. 2006).

20 The U-Pb zircon age for the onset of the oldest metamorphic event was estimated using the
21 TuffZirc method, developed by Ludwig and Mundil (2002), which calculates the median by choosing the
22 largest set of concordant analyses that are statistically coherent. The best estimate obtained for this event
23 is 489.58 (+ 12.15 - 6.76) Ma, obtained by pooling together only six of sixteen analyses (Fig. 16). The
24 510-380 Ma zircon aliquot shows a clear correlation between its cathodoluminescence texture and its
25 geochemistry and could be also related to shielded population of "metamorphic" zircon grains within
26 garnets (Fig. 4 e). The age recorded in the migmatitic paragneisses is thought to correspond to a
27 metamorphic event, dated in the Early Ordovician (~490 Ma), and is in very good agreement with upper
28 high-P/high-T dates of equivalent units carried out during previous studies (Kuijper, 1979; Peucat et al.,
29 1990; Fernández-Suárez et al., 2002, 2007). This age also coincides with those obtained from
30 intermediate-P units, where large plutons were emplaced and there is a lack of later high-P/high-T
31 metamorphism during the Devonian. The westernmost upper intermediate-P units of the Órdenes
32 Complex underwent a granulite-facies metamorphism dated between ca. 500 and 485 Ma,
33 contemporaneous with the intrusion of massive gabbros and granodiorites related to Cambrian magmatic
34 arc activity (Abati et al. 1999, 2003, 2007, 1999; Andonaegui et al., 2002, 2012, 2016; Castañeiras et
35 al., 2002, 2010). The granulite-facies metamorphism is associated with heating produced by the
36 intrusions, accompanied by a quick burial, almost coeval with igneous emplacement (Abati et al., 2003;
37 Castañeiras, 2005; Fernández-Suárez et al., 2007).

38 Clearly, the metamorphic event recorded in some zircons is pre-Variscan and it is therefore
39 independent of the high-P/high-T granulite-facies metamorphism that occurred during the Early-Middle
40 Devonian that has been identified in the underlying upper units, such as in Sobrado with 660-770°C and
41 13-17 kbar (Arenas and Martínez Catalán, 2002), or 750-850°C and 12-15 kbar (Benítez-Pérez, 2017).
42 Thus, not only was the pre-Variscan metamorphism followed by a decompression stage that was
43 associated with partial melting (Fernández-Suárez et al., 2002), but also, later Devonian metamorphism
44 and decompression during exhumation occurred, leading to partial melting in paragneisses and basic
45 granulites (Fernández-Suárez et al., 2007). As the zircon composition and microstructural setting clearly
46 suggests, the notable slope observed in the TuffZirc plot from 489 to 380 Ma (Fig. 16) is the result of
47 these exhumation, burial and new exhumation processes accompanied by partial melting, in which the
48 shielding role of garnet has played an important role.

49 6. Conclusions

1 This study provides new age constraints on the processes that have affected the Sobrado unit, part
2 of the Órdenes Complex, and allows some correlation with events recognized in other parts of the
3 allochthonous high-P/high-T complexes of NW Iberia. Titanite, monazite and zircon dating, together with
4 REE analyses have been combined together in these rocks for the first time in order to carry out a
5 geochronological investigation of the amphibolites and paragneisses.

6 According to the analyses, the youngest ages recorded by the metamorphic zircons are coherent
7 with the concordia monazite age obtained from seventy-six analyses in the paragneisses. The
8 microtextural setting of both metamorphic zircon and monazite along the HP-HT main foliation support
9 that interpretation. Therefore, the Middle Devonian age (~380 Ma) represents the minimum age of the
10 last Sobrado metamorphic event under high-P granulite-facies conditions and represents the first stages of
11 the Variscan orogeny in this part of Iberia. Dating of metamorphic titanite in the amphibolite yields a Late
12 Devonian age (~365 Ma) and is associated with very homogeneous REE patterns suggesting the
13 prolongation of the exhumation process in the Sobrado unit, reaching amphibolite-facies metamorphic
14 conditions. In zircon, there is a strong relationship between their textures, as seen in cathodoluminescence
15 images (CL), REE patterns and $^{206}\text{Pb}/^{238}\text{U}$ ages. Metamorphic zircon defines an Early Ordovician age
16 (~490 Ma) although showing a large dispersion. This date is linked to the first pre-Variscan granulite-
17 facies metamorphism seen in Sobrado unit under intermediate-P conditions, and it is interpreted to be
18 related to the intrusion of basic and intermediate composition rocks, and coeval with burial in a magmatic
19 arc context. Microstructural analysis of zircon, monazite and titanite provide complementary
20 microtextural context to understand the origin of this population mixture. In situ dating should be
21 conducted to confirm some textural relationships in the future.

22 The maximum depositional age of the Sobrado unit is suggested to be late Cambrian based on the
23 age of the youngest inherited zircon (511 Ma). From the youngest set of inherited zircon, two ages can be
24 obtained (546 and 526 Ma), pointing to the formation of a peri-Gondwana magmatic arc. The protoliths
25 of inherited zircon older than 1000 Ma from the Sobrado unit are found in other Iberian complexes and
26 are thought to be related to sources mainly in the West African craton.

27
28 *Data availability*
29

30 The data are not publicly accessible
31

32 *Supplement*
33

34 There is no supplement related to this article.
35

36 *Author contributions*
37

38 JMBP, PC, JGB and JRMC contributed equally to the field, experimental and elaboration of the
39 manuscript. AKC contributes to U-Pb-REE acquisition and data reduction and RH participated in the
40 writing of the text and the geological interpretation.
41

42 *Competing interests*
43

44 The authors declare that they have no conflict of interest.
45

46 **Acknowledgements**

47 This paper has been funded by the research projects CGL2011-22728 and CGL2016-78560-P of
48 the Spanish Ministry of Economy, Industry and Competitiveness, as part of the National Program of
49 Projects in Fundamental Research. JMBP appreciate financial support by the Spanish Ministry of
50 Economy, Industry and Competitiveness though the Formación de Profesional Investigador grant FPI
51 2013-2016 (BES-2012-059893). JGB appreciates financial support by the Spanish Ministry of Science

1 and Innovation through the IEDI-2016-00691 fellowship. We kindly appreciate excellent reviews from M.
2 Zucali, F. Rossetti, P. Ayarza and an anonymous referee which contributed to improve the manuscript.

3

4 **References**

- 5 Abati, J., Dunning, G.R., Arenas, R., Díaz García, F., González Cuadra, P., Martínez Catalán, J.R.,
6 Andonaegui, P., 1999. Early Ordovician orogenic event in Galicia (NW Spain): Evidence from U-Pb ages
7 in the uppermost unit of the Ordenes Complex. *Earth and Planetary Science Letters* 165, 213–228.
8 doi:10.1016/S0012-821X(98)00268-4
- 9 Abati, J., Arenas, R., Martínez Catalán, J.R., Díaz García, F., 2003. Anticlockwise P-T Path of Granulites
10 from the Monte Castelo Gabbro (Ordenes Complex, NW Spain). *Journal of Petrology* 44, 305–327.
11 doi:10.1093/petrology/44.2.305
- 12 Abati, J., Castiñeiras, P., Arenas, R., Fernández-Suárez, J., Barreiro, J.G., Wooden, J.L., 2007. Using
13 SHRIMP zircon dating to unravel tectonothermal events in arc environments. The early Palaeozoic arc of
14 NW Iberia revisited. *Terra Nova* 19, 432–439. doi:10.1111/j.1365-3121.2007.00768.x
- 15 Abati, J., Gerdes, A., Suárez, J.F., Arenas, R., Whitehouse, M.J., Fernández, R.D., 2010. Magmatism and
16 early-Variscan continental subduction in the northern Gondwana margin recorded in zircons from the
17 basal units of Galicia, NW Spain. *Bulletin of the Geological Society of America* 122, 219–235.
18 doi:10.1130/B26572.1
- 19 Aerden, D.G.A.M., 2004. Correlating deformation in Variscan NW-Iberia using porphyroblasts;
20 implications for the Ibero-Armorican Arc. *Journal of Structural Geology* 26, 177–196.
21 doi:10.1016/S0091-8141(03)00070-1
- 22 Albert, R., Arenas, R., Gerdes, A., Sánchez-Martínez, S., Fernández-Suárez, J., Fuenlabrada, J.M., 2015.
23 Provenance of the Variscan Upper Allochthon (Cabo Ortegal Complex, NW Iberian Massif). *Gondwana*
24 *Research* 28, 1434–1448. doi:10.1016/j.gr.2014.10.016
- 25 Aleinikoff, J.N., Schenck, W.S., Plank, M.O., Srogi, L.A., Fanning, C.M., Kamo, S.L., Bosbyshell, H.,
26 2006. Deciphering igneous and metamorphic events in high-grade rocks of the Wilmington complex,
27 Delaware: Morphology, cathodoluminescence and backscattered electron zoning, and SHRIMP U-Pb
28 geochronology of zircon and monazite. *Bulletin of the Geological Society of America* 118, 39–64.
29 doi:10.1130/B25659.1
- 30 Aleinikoff, J.N., Wintsch, R.P., Tollo, R.P., Unruh, D.M., Fanning, C.M., Schmitz, M.D., 2007. Ages and
31 origins of rocks of the Killingworth dome, south-central Connecticut: Implications for the tectonic
32 evolution of southern New England. *American Journal of Science* 307, 63–118. doi:10.2475/01.2007.04
- 33 Álvarez-Valero, A.M., Gómez-Barreiro, J., Alampi, A., Castineiras, P., Martínez Catalán, J.R., 2014.
34 Local isobaric heating above an extensional detachment in the middle crust of a Variscan allochthonous
35 terrane (Ordenes complex, NW Spain). *Lithosphere* 6, 409–418. doi:10.1130/L369.1
- 36 Andonaegui, P., Castiñeiras, P., González Cuadra, P., Arenas, R., Sánchez Martínez, S., Abati, J., Díaz
37 García, F., Martínez Catalán, J.R., 2012. The Corredoiras orthogneiss (NW Iberian Massif):
38 Geochemistry and geochronology of the Paleozoic magmatic suite developed in a peri-Gondwanan arc.
39 *Lithos* 128–131, 84–99. doi:10.1016/j.lithos.2011.11.005
- 40 Andonaegui, P., González Del Tánago, J., Arenas, R., Abati, J., Martínez Catalán, J.R., Peinado, M., Díaz
41 García, F., 2002. Tectonic setting of the Monte Castelo gabbro (Ordenes Complex, northwestern Iberian
42 Massif): Evidence for an arc-related terrane in the hanging wall to the Variscan suture. *Special Paper of*
43 *the Geological Society of America* 364, 37–56. doi:10.1130/0-8137-2364-7.37

- 1 Andonaegui, P., Sánchez-Martínez, S., Castiñeiras, P., Abati, J., Arenas, R., 2016. Reconstructing
2 subduction polarity through the geochemistry of mafic rocks in a Cambrian magmatic arc along the
3 Gondwana margin (Órdenes Complex, NW Iberian Massif). International Journal of Earth Sciences 105,
4 713–725. doi:10.1007/s00531-015-1195-x
- 5 Arenas, R., Martínez Catalán, J.R., 2002. Prograde development of corona textures in metagabbros of the
6 Sobrado unit (Órdenes Complex, northwestern Iberian Massif). Geological Society of America Special
7 Pa, 73–88. doi:10.1130/0-8137-2364-7.73
- 8 Bacon, C.R., Vazquez, J.A., Wooden, J.L., 2012. Peninsular terrane basement ages recorded by Paleozoic
9 and Paleoproterozoic zircon in gabbro xenoliths and andesite from Redoubt volcano, Alaska. Bulletin of
10 the Geological Society of America 124, 24–34. doi:10.1130/B30439.1
- 11 Ballèvre, M., Martínez Catalán J.R., López-Carmona, A., Pitra, P., Abati, J., Díez Fernández, R.,
12 Ducassou, C., Arenas, R., Bosse, V., Castiñeiras, P., Fernández-Suárez, J., Gómez Barreiro, J., Paquette,
13 J.-L., Peucat, J-J., Poujol, M., Ruffet, G. and Sánchez Martínez, S., 2014. Correlation of the nappe stack in
14 the Ibero-Armorican arc across the Bay of Biscay: a joint French–Spanish project. Geological Society,
15 London, Special Publications, 405, .doi: 10.1144/SP405.13
- 16 Barth, A.P., Wooden, J.L., 2010. Coupled elemental and isotopic analyses of polygenetic zircons from
17 granitic rocks by ion microprobe, with implications for melt evolution and the sources of granitic
18 magmas. Chemical Geology 277, 149–159. doi:10.1016/j.chemgeo.2010.07.017
- 19 Belousova, E.A., Griffin, W.L., O'Reilly, S.Y., Fisher, N.I., 2002. Igneous zircon: trace element
20 composition as an indicator of source rock type. Contributions to Mineralogy and Petrology 143, 602–
21 622. doi:10.1007/s00410-002-0364-7
- 22 Benítez-Pérez, J.M., 2017. Quantitative study of texture in tectonites by diffraction. Contribution to
23 seismic anisotropy and orogenic rheology. University of Salamanca (PhD. Thesis). Spain.
- 24 Buick, I.S., Clark, C., Rubatto, D., Hermann, J., Pandit, M., Hand, M., 2010. Constraints on the
25 Proterozoic evolution of the Aravalli-Delhi Orogenic belt (NW India) from monazite geochronology and
26 mineral trace element geochemistry. Lithos 120, 511–528. doi:10.1016/j.lithos.2010.09.011
- 27 Castiñeiras, P., Andonaegui, P., Arenas, R., Martínez Catalán, J., 2002. Descripción y resultados
28 preliminares del plutón compuesto de San Xiao, Complejo de Cabo Ortegal (noroeste del Macizo
29 Ibérico). Geogaceta 32, 111–114.
- 30 Castiñeiras, P., 2005. Origen y evolución tectonotermal de las unidades de O Pino y Cariño (Complejos
31 Alóctonos de Galicia). Laboratorio Xeolóxico de Laxe, Serie Nova Terra, 28, A Coruña.
- 32 Castiñeiras, P., García, F.D., Gómez-Barreiro, J., 2010. REE-assisted U-Pb zircon age (SHRIMP) of an
33 anatexic granodiorite: Constraints on the evolution of the A Silva granodiorite, Iberian allochthonous
34 complexes. Lithos 116, 153–166. doi:10.1016/j.lithos.2010.01.013
- 35 Castiñeiras, P., Navidad, M., Casas, J.M., Liesa, M., Carreras, J., 2011. Petrogenesis of Ordovician
36 Magmatism in the Pyrenees (Albera and Canigó Massifs) Determined on the Basis of Zircon Minor and
37 Trace Element Composition. The Journal of Geology 119, 521–534. doi:10.1086/660889
- 38 Chen, R.X., Zheng, Y.F., Xie, L., 2010. Metamorphic growth and recrystallization of zircon: Distinction
39 by simultaneous in-situ analyses of trace elements, U-Th-Pb and Lu-Hf isotopes in zircons from eclogite-
40 facies rocks in the Sulu orogen. Lithos 114, 132–154. doi:10.1016/j.lithos.2009.08.006
- 41 Cheng, H., King, R.L., Nakamura, E., Vervoort, J.D., Zheng, Y.F., Ota, T., Wu, Y.B., Kobayashi, K.,
42 Zhou, Z.Y., 2009. Transitional time of oceanic to continental subduction in the Dabie orogen: Constraints
43 from U-Pb, Lu-Hf, Sm-Nd and Ar-Ar multichronometric dating. Lithos 110, 327–342.
44 doi:10.1016/j.lithos.2009.01.013

- 1 Cherniak, D.J., 2006. Zr diffusion in titanite. Contributions to Mineralogy and Petrology 152, 639–647.
2 doi:10.1007/s00410-006-0133-0
- 3 Corfu, F., Hanchar, J.M., Hoskin, P.W.O., Kinny, P.D., 2003. Atlas of Zircon Textures, in: Hanchar,
4 J.M., Hoskin, P.W.O. (Eds.), Zircon. Reviews in Mineralogy and Geochemistry. Mineralogical Society of
5 America, pp. 468–500.
- 6 Corrie, S.L., Kohn, M.J., 2008. Trace-element distributions in silicates during prograde metamorphic
7 reactions : implications for monazite formation 451–464. doi:10.1111/j.1525-1314.2008.00769.x
- 8 Dallmeyer, R.D., Martínez Catalán, J.R., Arenas, R., Gil Ibarguchi, J.I., Gutiérrez-Alonso, G., Farias, P.,
9 Bastida, F., Aller, J., 1997. Diachronous Variscan tectonothermal activity in the NW Iberian Massif:
10 Evidence from $^{40}\text{Ar}/^{39}\text{Ar}$ dating of regional fabrics. Tectonophysics 277, 307–337. doi:10.1016/S0040-
11 1951(97)00035-8
- 12 Dallmeyer, R.D., Ribeiro, A., Marques, F., 1991. Polyphase Variscan emplacement of exotic terranes
13 (Morais and Bragança Massifs) onto Iberian successions: Evidence from $^{40}\text{Ar}/^{39}\text{Ar}$ mineral ages. Lithos
14 27, 133–144. doi:10.1016/0024-4937(91)90025-G
- 15 DeWolf, C.P., Belshaw, N., O’Nions, R.K., 1993. A metamorphic history from micron-scale
16 $^{207}\text{pb}/^{206}\text{pb}$ chronometry of Archean monazite. Earth and Planetary Science Letters 120, 207–220.
- 17 Dias da Silva, I., Valverde-Vaquero, P., González-Clavijo, E., Díez-Montes, A. y Martínez Catalán, J. R.
18 2014. Structural and stratigraphical significance of U–Pb ages from the Mora and Saldanha volcanic
19 complexes (NE Portugal, Iberian Variscides). In: Schulmann, K., Martínez Catalán, J. R., Lardeaux, J.
20 M., Janousek, V. & Oggiano, G. (eds) The Variscan Orogeny: Extent, Timescale, the Formation of the
21 European Crust. Geological Society, London, Special Publications, 405. First published online February
22 25, 2014, <http://dx.doi.org/10.1144/SP405.3>
- 23 Díaz García, F., Martínez Catalán, J.R., Arenas, R., González Cuadra, P., 1999. Structural and kinematic
24 analysis of the Corredoiras detachment: evidence for early Variscan synconvergent extension in the
25 Ordenes Complex, NW Spain. International Journal of Earth Sciences 88, 337–351.
- 26 Dickinson, W.R., Gehrels, G.E., 2009. Use of U-Pb ages of detrital zircons to infer maximum
27 depositional ages of strata: A test against a Colorado Plateau Mesozoic database. Earth and Planetary
28 Science Letters 288, 115–125. doi:10.1016/j.epsl.2009.09.013
- 29 Díez Fernández, R., Catalán, J.R.M., Gerdes, A., Abati, J., Arenas, R., Fernández-Suárez, J., 2010. U-Pb
30 ages of detrital zircons from the Basal allochthonous units of NW Iberia: Provenance and paleoposition
31 on the northern margin of Gondwana during the Neoproterozoic and Paleozoic. Gondwana Research 18,
32 385–399. doi:10.1016/j.gr.2009.12.006
- 33 Díez Fernández, R., Martínez Catalán, J.R., Arenas, R., Abati, J., Gerdes, A., Fernández-Suárez, J., 2012.
34 U-Pb detrital zircon analysis of the lower allochthon of NW Iberia: age constraints, provenance and links
35 with the Variscan mobile belt and Gondwanan cratons. Journal of the Geological Society 169, 655–665.
36 doi:10.1144/jgs2011-146
- 37 Egal, E., Thiéblemont, D., Lahondère, D., Guerrot, C., Costea, C.A., Iliescu, D., Delor, C., Goujou, J.C.,
38 Lafon, J.M., Tegyey, M., Diaby, S., Kolié, P., 2002. Late Eburnean granitization and tectonics along the
39 western and northwestern margin of the Archean K??n??ma-Man domain (Guinea, West African Craton).
40 Precambrian Research 117, 57–84. doi:10.1016/S0301-9268(02)00060-8
- 41 Ennih, N., Liegeois, J.-P., 2008. The boundaries of the West African craton, with special reference to the
42 basement of the Moroccan metacratonic Anti-Atlas belt. The Boundaries of the West African Craton 1–
43 17. doi:10.1144/SP297.1
- 44 Farias, P., Gallastegui, G. et al. 1987. Aportaciones al conocimiento de la litoestratigrafía y estructura de
45 Galicia Central. Memo’rias da Faculdade de Ciências, Universidade do Porto, 1, 411–431.

- 1 Fernández-Suárez, J., Arenas, R., Abiati, J., Martínez Catalán, J.R., Whitehouse, M., Jeffries, T., 2007.
2 U-Pb chronometry of polymetamorphic high-pressure granulites: An example from the allochthonous
3 terranes of the NW Iberian Variscan belt. Geological Society of America Memoir, 469–488.
4 doi:10.1130/2007.1200(24).
- 5 Fernández-Suárez, J., Corfu, F., Arenas, R., Marcos, A., Martínez Catalán, J.R., Díaz García, F., Abati, J.,
6 Fernández, F.J., 2002. U-Pb evidence for a polyorogenic evolution of the HP-HT units of the NW Iberian
7 Massif. Contributions to Mineralogy and Petrology 143, 236–253. doi:10.1007/s00410-001-0337-2
- 8 Fernández-Suárez, J., Garcia, F.D., Jeffries, T.E., Arenas, R., 2003. Constraints on the provenance of the
9 uppermost allochthonous terrane of the NW Iberian Massif: inferences from detrital zircon U-Pb ages.
10 Terra Nova 15, 138–144.
- 11 Franz, G., Spear, F.S., 1985. Aluminous Titanite (sphene) from the eclogite zone, south-central Tauern
12 window, Austria. Chemical Geology 50, 33–46.
- 13 Frost, B.R., Chamberlain, K.R., Schumacher, J.C., 2000. Sphene (titanite): phase relations and role as a
14 geochronometer. Chemical Geology 172, 131–148.
- 15 Fuenlabrada, J., Arenas, R., Sánchez-Martínez, S., Díaz García, F., Castiñeiras, P., 2010. A peri-
16 Gondwanan arc in NW Iberia I: Isotopic and geochemical constraints on the origin of the arc-A
17 sedimentary approach. Gondwana Research 17, 338–351. doi:10.1016/j.gr.2009.09.007
- 18 Gagnevin, D., Daly, J.S., 2010. Zircon texture and chemical composition as a guide to magmatic
19 processes and mixing in a granitic environment and coeval volcanic system. doi:10.1007/s00410-009-
20 0443-0
- 21 Gómez Barreiro, J., Wijbrans, J.R., Castiñeiras, P., Martínez Catalán, J.R., Arenas, R., Díaz García, F.
22 and Abati, J., 2006. $^{40}\text{Ar}/^{39}\text{Ar}$ laserprobe dating of mylonitic fabrics in a polyorogenic terrane of NW
23 Iberia. Journal of the Geological Society, 163(1), pp.61-73. <https://doi.org/10.1144/0016-764905-012>.
- 24 Gómez-Barreiro, J., Martínez Catalán, J.R., Arenas, R., Castiñeiras, P., Abati, J., Díaz García, F.,
25 Wijbrans, J.R., 2007. Tectonic evolution of the upper allochthon of the Órdenes complex (northwestern
26 Iberian Massif): Structural constraints to a polyorogenic peri-Gondwanan terrane. Geological Society of
27 America 423, 315–332. doi:10.1130/2007.2423(15).
- 28 Goncalves, P., Williams, M.L., Jercinovic, M.J., 2005. Electron-microprobe age mapping of monazite.
29 American Mineralogist 90, 578–585. doi:10.2138/am.2005.1399
- 30 Grimes, C.B., Wooden, J.L., Cheadle, M.J., John, B.E., 2015. “Fingerprinting” tectono-magmatic
31 provenance using trace elements in igneous zircon. Contributions to Mineralogy and Petrology 170, 1–26.
32 doi:10.1007/s00410-015-1199-3
- 33 Gutiérrez-Alonso, G., Fernández-Suárez, J., Jeffries, T.E., Jenner, G.A., Tubrett, M.N., Cox, R., Jackson,
34 S.E., 2003. Terrane accretion and dispersal in the northern Gondwana margin. An Early Paleozoic
35 analogue of a long-lived active margin. Tectonophysics 365, 221–232. doi:10.1016/S0040-
36 1951(03)00023-4
- 37 Hacker, B.R., Kylander-clark, A.R.C., Holder, R., Andersen, T.B., Peterman, E.M., Walsh, E.O.,
38 Munninkhuis, J.K., 2015. Monazite response to ultrahigh-pressure subduction from U – Pb dating by laser
39 ablation split stream. Chemical Geology 409, 28–41. doi:10.1016/j.chemgeo.2015.05.008
- 40 Hanchar, J.M., Westrenen, W. Van, 2007. Rare earth element behavior in zircon–melt systems. Elements
41 3, 37–42.
- 42 Harlov, D., Tropper, P., Seifert, W., Nijland, T., Förster, H.-J., 2006. Formation of Al-rich titanite
43 ($\text{CaTiSiO}_4 \text{ O} - \text{CaAlSiO}_4 \text{ OH}$) reaction rims on ilmenite in metamorphic rocks as a function of f H_2O
44 and f O_2 . Lithos 88, 72–84. doi:10.1016/j.lithos.2005.08.005

- 1 Hawkins, D.P., Bowring, S.A., 1997. U-Pb systematics of monazite and xenotime : case studies from the
2 Paleoproterozoic of the Grand Canyon, Arizona 87–103.
- 3 Hermann, J., Rubatto, D., 2003. Relating zircon and monazite domains to garnet growth zones : Age and
4 duration of granulite facies metamorphism in the Val Malenco lower crust. Journal of Metamorphic 21,
5 Issue 9. doi:10.1046/j.1525-1314.2003.00484.x
- 6 Hokada, T., Harley, S.L., 2004. Zircon growth in UHT leucosome: constraints from zircon-garnet rare
7 earth elements (REE) relations in Napier Complex, East Antarctica. Journal of Mineralogical and
8 Petrological Sciences 99, 180–190. doi:10.2465/jmps.99.180
- 9 Holder, R.M., Hacker, B.R., Kylander-clark, A.R.C., Cottle, J.M., 2015. Monazite trace-element and
10 isotopic signatures of (ultra) high-pressure metamorphism : Examples from the Western Gneiss Region,
11 Norway. Chemical Geology 409, 99–111. doi:10.1016/j.chemgeo.2015.04.021
- 12 Horstwood, M.S.A., Foster, G.L., Parrish, R.R., Noble, S.R., Nowell, G.M., 2003. Common-Pb corrected
13 in situ U–Pb accessory mineral geochronology by LA-MC-ICP-MS. The Royal Society of Chemistry 18,
14 837–846. doi:10.1039/b304365g
- 15 Hoskin, P.W.O., 2005. Trace-element composition of hydrothermal zircon and the alteration of Hadean
16 zircon from the Jack Hills, Australia. Geochimica et Cosmochimica Acta 69, 637–648.
17 doi:10.1016/j.gca.2004.07.006
- 18 Hoskin, P.W.O., Ireland, T.R., 2000. Rare earth element chemistry of zircon and its use as a provenance
19 indicator. Geology 28, 627–630. doi:10.1130/0091-7613(2000)28<627:RECOZ>2.0.CO
- 20 Hoskin, P.W.O., Schaltegger, U., 2003. The Composition of Zircon and Igneous and Metamorphic
21 Petrogenesis, in: Hanchar, J.M., Hoskin, P.W.O. (Eds.), Zircon. Reviews in Mineralogy and
22 Geochemistry. Mineralogical Society of America, pp. 27–62.
- 23 Jackson, S.E., Pearson, N.J., Griffin, W.L., Belousova, E.A., 2004. The application of laser ablation-
24 inductively coupled plasma-mass spectrometry to in situ U-Pb zircon geochronology. Chemical Geology
25 211, 47–69. doi:10.1016/j.chemgeo.2004.06.017
- 26 Ji, S., Martignole, J., 1994. Ductility of garnet as an indicator of extremely high temperature deformation.
27 Journal of Structural Geology 16, 985–996.
- 28 Kleinschrodt, R., Duyster, J., 2002. HT-deformation of garnet: an EBSD study on granulites from Sri
29 Lanka, India and the Ivrea Zone. Journal of Structural Geology 24, 1829–1844.
- 30 Kohn, M.J., Malloy, M.A., 2004. Formation of monazite via prograde metamorphic reactions among
31 common silicates : Implications for age determinations. Geochimica et cosmochimica Acta 68, 101–113.
32 doi:10.1016/S0016-7037(03)00258-8
- 33 Košler, J., Tubrett, M.N., Sylvester, P.J., 2001. Application of laser ablation ICP-MS to U-Th-Pb dating
34 of monazite. Geostandards Newsletter-the Journal of Geostandards and Geoanalysis 25, 375–386.
35 doi:10.1111/j.1751-908X.2001.tb00612.x
- 36 Kretz, R., 1983. Symbols for rock-forming minerals. American Mineralogist 68, 277–279.
37 doi:10.1016/0016-7037(83)90220-X
- 38 Kuijper, R.P., 1979. U-Pb systematic and petrogenetic evolution of infracrustal rocks in the Paleozoic
39 basement of Western Galicia, NW Iberia. WO Laboratory of Isotope Geology, Amsterdam.
- 40 Kylander-Clark, A.R.C., Hacker, B.R., Cottle, J.M., 2013. Laser-ablation split-stream ICP
41 petrochronology. Chemical Geology 345, 99–112. doi:10.1016/j.chemgeo.2013.02.019

- 1 Lesnov, F.P., 2013. Consistent patterns of rare earth element distribution in accessory minerals from
2 rocks of mafic-ultramafic complexes. Central European Journal of Geosciences 5, 112–173.
3 doi:10.2478/s13533-012-0121-z
- 4 Linnemann, U., Gerdes, A., Hofmann, M., Marko, L., 2014. The Cadomian Orogen: Neoproterozoic to
5 Early Cambrian crustal growth and orogenic zoning along the periphery of the West African Craton-
6 Constraints from U-Pb zircon ages and Hf isotopes (Schwarzburg Antiform, Germany). Precambrian
7 Research 244, 236–278. doi:10.1016/j.precamres.2013.08.007
- 8 Ludwig, K.R., 1998. On the Treatment of Concordant Uranium-Lead Ages. *Geochimica et*
9 *Cosmochimica Acta* 62, 665–676. doi:10.1016/S0016-7037(98)00059-3
- 10 Ludwig, K.R., Mundil, R., 2002. Extracting reliable U–Pb ages and errors from complex populations of
11 zircons from Phanerozoic tuffs. *Geochimica et Cosmochimica Acta* 66, 463.
- 12 Ludwig, K.R., 2012. User's Manual for ISOPLOT version 3.75. A Geochronological Toolkit for
13 Microsoft Excel. Berkeley Geochronology Center.
- 14 Martínez Catalán, J.R., Arenas, R., Díaz García, F., Abati, J., 1999. Allochthonous Units in the Variscan
15 Belt of NW Iberia: Terranes and Accretionary History, in: Sinha, A.K. (Ed.), Basement Tectonics 13:
16 Proceedings of the Thirteenth International Conference on Basement Tectonics Held in Blacksburg,
17 Virginia, U.S.A., June 1997. Springer Netherlands, Dordrecht, pp. 65–84. doi:10.1007/978-94-011- 4800-
18 9_5
- 19 Martínez Catalán, J.R., Fernández-Suárez, J., Jenner, G.A., Belousova, E., Díez Montes, A., 2004,
20 Provenance constraints from detrital zircon U–Pb ages in the NW Iberian Massif: implications for
21 Paleozoic plate configuration and Variscan evolution. *J. Geol. Soc. London*, 161, 461–473.
22 doi:10.1144/0016-764903-054
- 23 Martínez Catalán, J.R., Arenas, R., Abati, J., Sánchez Martínez, S., Díaz García, F., Fernández Suárez, J.,
24 González Cuadra, P., Castiñeiras, P., Gómez Barreiro, J., Díez Montes, A., González Clavijo, E., Rubio
25 Pascual, F.J., Andonaegui, P., Jeffries, T.E., Alcock, J.E., Díez Fernández, R., López Carmona, A., 2009.
26 A rootless suture and the loss of the roots of a mountain chain: The Variscan belt of NW Iberia. *Comptes
27 Rendus Geoscience* 341, 114–126. doi:10.1016/j.crte.2008.11.004
- 28 Martínez Catalán, J.R., 2011. Are the oroclines of the Variscan belt related to late Variscan strike-slip
29 tectonics? *Terra Nova* 23, 241–247. doi:10.1111/j.1365-3121.2011.01005.x
- 30 Martínez Catalán, J.R., 2012. The Central Iberian arc, an orocline centered in the Iberian Massif and some
31 implications for the Variscan belt. *International Journal of Earth Sciences* 101, 1299–1314.
32 doi:10.1007/s00531-011-0715-6
- 33 McDonough, W.F., Sun, S.S., 1995. The composition of the Earth. *Chemical Geology* 120, 223–253.
34 doi:10.1016/0009-2541(94)00140-4
- 35 Möller, A., O'Brien, P.J., Kennedy, A., Kröner, A., 2002. Polyphase zircon in ultrahigh-temperature
36 granulites (Rogaland, SW Norway): Constraints for Pb diffusion in zircon. *Journal of Metamorphic
37 Geology* 20, 727–740. doi:10.1046/j.1525-1314.2002.00400.x
- 38 Mottram, C.M., Warren, C.J., Regis, D., Roberts, N.M.W., Harris, N.B.W., Argles, T.W., Parrish, R.R.,
39 2014. Developing an inverted barrovian sequence; insights from monazite petrochronology. *Earth and
40 Planetary Science Letters* 403, 418–431. doi:10.1016/j.epsl.2014.07.006
- 41 Mulrooney, D., Rivers, T., 2005. Redistribution of the rare-earth elements among coexisting minerals in
42 metamafic rocks across the epidote-out isograd: An example from the St. Anthony Complex, northern
43 Newfoundland, Canada. *Canadian Mineralogist* 43, 263–294. doi:10.2113/gscanmin.43.1.263

- 1 Nasdala, L., Zhang, M., Kempe, U., Panczer, G., Gaft, M., Andrus, M., Plötze, M., 2003. Spectroscopic
2 methods applied to zircon, in: Hanchar, J.M., Hoskin, P.W.O. (Eds.), Zircon. Reviews in Mineralogy and
3 Geochemistry. Mineralogical Society of America, pp. 427–467.
- 4 Ordóñez Casado, B., 1998. Geochronological studies of the pre-Mesozoic basement of the Iberian
5 Massif: the Ossa Morena zone and the Allochthonous Complexes within the Central Iberian zone. PhD
6 Thesis, Swiss Federal Institute of Technology, Zürich, Switzerland, 235 pp., doi:10.3929/ethz-a-
7 002017279
- 8 Ordóñez Casado, B., Gebauer, D., Schäfer, H.J., Ibarguchi, J.I.G., Peucat, J.J., 2001. A single Devonian
9 subduction event for the HP/HT metamorphism of the Cabo Ortegal complex within the Iberian Massif.
10 Tectonophysics 332, 359–385. doi:10.1016/S0040-1951(00)00210-9
- 11 Pablo Maciá, J.G. de, and Martínez Catalán, J.R. 1984. Estructura, petrología y evolución de la región de
12 Sobrado de los Monjes (La Coruña). Cuadernos do Laboratorio Xeolóxico de Laxe 7, 103–124.
- 13 Palin, R.M., Searle, M.P., Waters, D.J., Parrish, R.R., Roberts, N.M.W., Horstwood, M.S.A., Yeh, M.W.,
14 Chung, S.L., Anh, T.T., 2013. A geochronological and petrological study of anatectic paragneiss and
15 associated granite dykes from the Day Nui Con Voi metamorphic core complex, North Vietnam:
16 Constraints on the timing of metamorphism within the Red River shear zone. Journal of Metamorphic
17 Geology 31, 359–387. doi:10.1111/jmg.12025
- 18 Passchier, C. W., and Trouw, R. A. (2005). Microtectonics. Springer Science & Business Media.
19
- 20 Paton, C., Hellstrom, J., Paul, B., Woodhead, J., Hergt, J., 2011. Iolite: Freeware for the visualisation and
21 processing of mass spectrometric data. Journal of Analytical Atomic Spectrometry 26, 2508.
22 doi:10.1039/c1ja10172b
- 23 Peters, T.J., Ayers, J.C., Gao, S., Liu, X.M., 2013. The origin and response of zircon in eclogite to
24 metamorphism during the multi-stage evolution of the Huwan Shear Zone, China: Insights from Lu-Hf
25 and U-Pb isotopic and trace element geochemistry. Gondwana Research 23, 726–747.
26 doi:10.1016/j.gr.2012.05.008
- 27 Peucat, J.J., Bernard Griffiths, J., Ibarguchi, J.I.G., Dallmeyer, R.D., Menot, R.P., Cornichet, J., Ponce de
28 León, M.I., 1990. Geochemical and Geochronological Cross-Section of the Deep Variscan Crust - the
29 Cabo-Ortegal High-Pressure Nappe (Northwestern Spain). Tectonophysics 177, 263–292.
- 30 Peucat, J.J., Capdevila, R., Draren, A., Mahdjoub, Y., Kahoui, M., 2005. The Eglab massif in the West
31 African Craton (Algeria), an original segment of the Eburnean orogenic belt: Petrology, geochemistry and
32 geochronology. Precambrian Research 136, 309–352. doi:10.1016/j.precamres.2004.12.002
- 33 Potrel, A., Peucat, J.J., Fanning, C.M., 1998. Archean crustal evolution of the West African Craton:
34 example of the Amsaga Area (Reguibat Rise). U-Pb and Sm-Nd evidence for crustal growth and
35 recycling. Precambrian Research 90, 107–117. doi:10.1016/S0301-9268(98)00044-8
- 36 Ribeiro, A., Pereira, E. & Dias, R. 1990. Central-Iberian Zone. Allochthonous Sequences. Structure in the
37 Northwest of the Iberian Peninsula. In: Dallmeyer, R. D. y Martínez García, E. (eds) Pre-Mesozoic
38 Geology of Iberia. Springer, Berlin, 220–236.
- 39 Rubatto, D., Hermann, J., 2001. Exhumation as fast as subduction ? Geology 29, 3–6.
- 40 Rubatto, D., 2002. Zircon trace element geochemistry : distribution coefficients and the link between U-
41 Pb ages and metamorphism Zircon trace element geochemistry : partitioning with garnet and the link
42 between U – Pb ages and metamorphism. Chemical Geology 184, 123–138.
- 43 Rubatto, D., Hermann, R.G., Buick, I.S., 2006. Temperature and Bulk Composition Control on the
44 Growth of Monazite and Zircon During Low-pressure Anatexis (Mount Stafford , Central Australia).
45 Journal of Petrology 47, 1973–1996. doi:10.1093/petrology/egl033

- 1 Rubatto, D., Hermann, J., Berger, A., Engi, M., 2009. Protracted fluid-induced melting during Barrovian
2 metamorphism in the Central Alps. Contributions to Mineralogy and Petrology 158, 703–722.
3 doi:10.1007/s00410-009-0406-5
- 4 Rubatto, D., Chakraborty, S., Dasgupta, S., 2013. Timescales of crustal melting in the Higher Himalayan
5 Crystallines (Sikkim, Eastern Himalaya) inferred from trace element-constrained monazite and zircon
6 chronology. Contributions to Mineralogy and Petrology 165, 349–372. doi:10.1007/s00410-012-0812-y
- 7 Santos Zalduogui, J.F., Schärer, U., Gil Ibarguchi, J.I., 1995. Isotope constraints on the age and origin of
8 magmatism and metamorphism in the Malpica-Tuy allochthon, Galicia, NW Spain. Chemical Geology
9 121, 91–103. doi:10.1016/0009-2541(94)00123-P
- 10 Santos Zalduogui, J.F., Schärer, U., Gil Ibarguchi, J.I., Girardeau, J., 1996. Origin and evolution of the
11 Paleozoic Cabo Ortegal ultramafic-mafic complex (NW Spain): U-Pb, Rb-Sr and Pb-Pb isotope data.
12 Chemical Geology 129, 281–304. doi:10.1016/0009-2541(95)00144-1
- 13 Santos Zalduogui, J.F., Scharer, U., Gil Ibarguchi, J.I., Girardeau, J., 2002. Genesis of Pyroxenite-rich
14 Peridotite at Cabo Ortegal (NW Spain): Geochemical and Pb-Sr-Nd Isotope Data. J. Petrol. 43, 17–43.
15 doi:10.1093/petrology/43.1.17
- 16 Schaltegger, U., Fanning, C.M., Günter, D., Maurin, J.C., Schulmann, K., Gebauer, D., 1999. Growth,
17 annealing and recrystallization of zircon and preservation of monazite in high-grade metamorphism:
18 conventional and in-situ U-Pb isotope, cathodoluminescence and microchemical evidence. Contributions
19 to Mineralogy and Petrology 134, 186–201.
- 20 Schofield, D.I., Horstwood, M.S.A., Pitfield, P.E.J., Gillespie, M., Darbyshire, F., O'Connor, E.A.,
21 Abdouloye, T.B., 2012. U-Pb dating and Sm-Nd isotopic analysis of granitic rocks from the Tiris
22 Complex: New constraints on key events in the evolution of the Reguibat Shield, Mauritania. Precambrian
23 Research 204–205, 1–11. doi:10.1016/j.precamres.2011.12.008
- 24 Spear, F.S., 1981. An experimental study of hornblende stability and compositional variability in
25 amphibolite. American Journal of Science. doi:10.2475/ajs.281.6.697
- 26 Spear, F.S., Pyle, J.M., 2002. Apatite , Monazite , and Xenotime in Metamorphic Rocks, in: Kohn, M.J.,
27 Rakovan, J., Hughes, J.M. (Eds.), Phosphates: Geochemical, Geobiological, and Materials Importance.
28 Reviews in Mineralogy and Geochemistry. doi:10.2138/rmg.2002.48.7
- 29 Spencer, K.J., Hacker, B.R., Kylander-clark, A.R.C., Andersen, T.B., Cottle, J.M., Stearns, M.A., Poletti,
30 J.E., Seward, G.G.E., 2013. Campaign-style titanite U – Pb dating by laser-ablation ICP : Implications for
31 crustal flow , phase transformations and titanite closure. Chemical Geology 341, 84–101.
32 doi:10.1016/j.chemgeo.2012.11.012
- 33 Stearns, M.A., Cottle, J.M., Hacker, B.R., Kylander-Clark, A.R.C., 2016. Extracting thermal histories
34 from the near-rim zoning in titanite using coupled U-Pb and trace-element depth profiles by single-shot
35 laser-ablation split stream (SS-LASS) ICP-MS. Chemical Geology 422, 13–24.
36 doi:10.1016/j.chemgeo.2015.12.011
- 37 Stearns, M.A., Hacker, B.R., Ratschbacher, L., Rutte, D., Kylander-clark, A.R.C., 2015. Titanite
38 petrochronology of the Pamir gneiss domes: Implications for middle to deep crust exhumation and titanite
39 closure to Pb and Zr diffusion. Tectonics 34, 784–802. doi:10.1002/2014TC003774.Received
- 40 Stipska, P., Powell, R., Hacker, B.R., Holder, R., 2016. Uncoupled U / Pb and REE response in zircon
41 during the transformation of eclogite to mafic and intermediate granulite (Blansk y les , Bohemian
42 Massif). Journal of Meta 34, 551–572. doi:10.1111/jmg.12193
- 43 Storey, C.D., Smith, M.P., Jeffries, T.E., 2007. In situ LA-ICP-MS U – Pb dating of metavolcanics of
44 Norrbotten , Sweden : Records of extended geological histories in complex titanite grains. Chemical
45 Geology 240, 163–181. doi:10.1016/j.chemgeo.2007.02.004

- 1 Stübner, K., Grujic, D., Parrish, R.R., Roberts, N.M.W., Kronz, A., Wooden, J., Ahmad, T., 2014. Lithos
2 Monazite geochronology unravels the timing of crustal thickening in NW Himalaya. LITHOS 210–211,
3 111–128. doi:10.1016/j.lithos.2014.09.024
- 4 Tera, F., Wasserburg, G.J., 1972. U-Th-Pb systematics in three Apollo 14 basalts and the problem of
5 initial Pb in lunar rocks. Earth and Planetary Science Letters 14, 281–304. doi:10.1016/0012-
6 821X(72)90128-8
- 7 Terry, M.P., Hamilton, M.A., 2000. Monazite geochronology of UHP and HP metamorphism ,
8 deformation , and exhumation , Nordoyane ... doi:10.2138/am-2000-11-1208
- 9 Tomascak, P.B., Krogstad, E.J., Walker, R.J., 1996. U-Pb Monazite Geochronology of Granitic Rocks
10 from Maine: Implications for Late Paleozoic Tectonics in the Northern Appalachians. The Journal of
11 Geology 104, 185–195.
- 12 Verts, L.A., Frost, C.D., 1996. U-Pb sphene dating of metamorphism : the importance of sphene growth
13 in the contact aureole of the Red Mountain pluton , Laramie Mountains , Wyoming. Contributions to
14 Mineralogy and Petrology 125, 186–199.
- 15 Watson, E.B., Yan Liang, 1995. A simple model for sector zoning in slowly grown crystals: implications
16 for growth rate and lattice diffusion, with emphasis on accessory minerals in crustal rocks. American
17 Mineralogist 80, 1179–1187.
- 18 Whitehouse, M.J., Platt, A.E.J.P., 2003. Dating high-grade metamorphism - constraints from rare-earth
19 elements in zircon and garnet. Contributions to Mineralogy and Petrology 145, 61–74.
20 doi:10.1007/s00410-002-0432-z
- 21 Whitney, D. L., Evans, B. W. (2010). Abbreviations for names of rock-forming minerals. American
22 mineralogist, 95(1), 185-187. <https://doi.org/10.2138/am.2010.3371>
- 23 Wiedenbeck, M., Allé, P., Corfú, F., Griffin, W.L., Meier, M., Oberli, F., Quadt, A. Von, Roddick, J.C.,
24 Spiegel, W., 1995. Three Natural Zircon Standards for U-Th-Pb, Lu-Hf, Trace Element and REE
25 Analyses. Geostandards Newsletter 19, 1–23. doi:10.1111/j.1751-908X.1995.tb00147.x
- 26 Williams, M.L., Jercinovic, M.J., Hetherington, C.J., 2007. Microprobe Monazite Geochronology:
27 Understanding Geologic Processes by Integrating Composition and Chronology. Annual Review of Earth
28 and Planetary Sciences 35, 137–175. doi:10.1146/annurev.earth.35.031306.140228
- 29 Zeck, H.P., Wingate, M.T.D., Pooley, G.D., Ugidos, J.M., 2004. A Sequence of Pan-African and
30 Hercynian Events Recorded in Zircons from an Orthogneiss from the Hercynian Belt of Western Central
31 Iberia —an Ion Microprobe U– Pb Study 45, 1613–1629. doi:10.1093/petrology/egh026
- 32 Zeringue, J., Bowring, J.~F., McLean, N.~M., Pastor, F., 2014. Building Interactive Visualizations for
33 Geochronological Data. AGU Fall Meeting Abstracts.
- 34 Zhu, X.K., O’Nions, R.K., Belshaw, N.S., Gibb, A.J., 1997. Significance of in situ SIMS chronometry of
35 zoned monazite from the Lewisian granulites, northwest Scotland. Chemical Geology 5, 35–53.
- 36
- 37
- 38
- 39
- 40
- 41
- 42

1
2

3 FIGURE CAPTIONS

4 Figure 1. (a) Simplified map of the Variscan orogen in Europe with the location of the Órdenes Complex.
5 (b) Map of the Órdenes Complex with indication of the main units and tectonic contacts. Extensional
6 detachments are labeled: BPSD, Bembibre-Pico Sacro system; CD: Corredoiras; FD, Fornás; PCD, Ponte
7 Carreira. Fig. 2 location indicated.

8

9 Figure 2. Geological map of the study area and location of the samples, modified from Arenas and
10 Martínez Catalán (2002): (a) Location of the Órdenes complex within the Iberian massif. (b) Sobrado
11 Unit map, indicating units and horses. (c) Cross-section in WNW-ESE direction and (d) SW-NE and
12 SSW-NNE direction of the Sobrado antiform. Sample location are indicated.

13 Figure 3. Fine grained amphibolites (sample JBP-71-21) from the basal mylonitic band in the Sobrado
14 Upper horse. (a) Hornblende-plagioclase mixtures and titanite with preferred orientation, defining the
15 mylonitic fabric. (b) Main fabric surrounding a garnet porphyroblast. Note titanite is the Ti phase in the
16 mylonitic fabric but ilmenite grains have been preserved inside the garnet. The position of (c) is indicated
17 by a white dashed square. (c) Garnet inclusions from (b) where ilmenite inclusions show a progressive
18 breakdown into titanite (Ilm>Tit). Note ilmenite inclusions inside pristine garnet areas show no evidence
19 of transformation. (d) Inclusions of rutile inside titanite and partial transformation of plagioclase into
20 zoisite. (e) Titanite mineral fish showing a top-to-the NNE shear sense. Small ilmenite inclusions are
21 visible in titanite. (f) Retrogression of plagioclase into zoisite and ilmenite inclusions inside titanite grains
22 parallel to the main foliation. All micrographs in plane-polarized light (PPL). (Mineral abbreviations
23 after Whitney and Evans, 2010; Hbl: hornblende, Tit: titanite, Ilm: ilmenite, Rt: rutile, Pl: plagioclase,
24 Zo: zoisite, Grt: garnet).

25 Figure 4. Granulite facies migmatitic paragneiss from the Sobrado Middle horse (Fig. 2). (a) General
26 microstructure where leucosome bands and preferred orientation of elongated garnets, biotite, rutile and
27 kyanite define the foliation. (b) Zircon elongated grain in recrystallized leucosome domain. Main
28 inclusions in garnet include rutile, ilmenite and zircon (PPL) and (c) Cross-polarized light (CPL). (d)
29 Monazite and zircon surrounded grain in the leucosome domain. (e) Surrounding elongated grain of
30 zircon included in a garnet. (f) Plastically deformed garnet (sigmoidal grain) in a leucosome. Zircon and
31 monazite are found in the quartz-rich area around the garnet. (g) Sigmoidal garnet in a leucosome.
32 Inclusions of prismatic and bipiramidal zircons and rutile are observed. (h) Monazite grain in a garnet
33 pressure shadow with biotite. Ky: kyanite, Bt: biotite, Qtz: quartz, Kfs: K-feldspar, Pl: plagioclase, Rt:
34 rutile, Zrn: zircon, Mnz: monazite, Grt: garnet.

35 Figure 5. (a) Monazite grain compositional maps in paragneiss with a 30% thorium variation. Location
36 and spot numbers (46 and 47) are indicated, as well as the $^{206}\text{Pb}/^{238}\text{U}$ age and error ($\pm 2\sigma$). (b)
37 Chondrite-normalized rare earth element (REE) patterns for the same monazites in (a).

38 Figure 6. Cathodoluminescence (CL) images with the location of the analyzed spots for selected zircon
39 grains.

40 Figure 7. (a) Tera-Wasserburg diagram showing distribution of analysed titanites ($n = 51$) from Sobrado
41 amphibolite (JB-71-21). The rejected analyses are represented by gray ellipses. The ellipses represent
42 the $^{207}\text{Pb}/^{206}\text{Pb}$ and $^{238}\text{U}/^{206}\text{Pb}$ errors ($\pm 2\sigma$). (b) Chondrite-normalized rare earth element (REE) patterns
43 for the same titanites.

44 Figure 8. (a) Tera-Wasserburg diagram showing distribution of analysed monazites ($n = 76$) from
45 Sobrado paragneiss (JB-71-15). The rejected analyses are represented by gray ellipses. The ellipses

1 represent the $^{207}\text{Pb}/^{206}\text{Pb}$ and $^{238}\text{U}/^{206}\text{Pb}$ errors ($\pm 2\sigma$). (b) Chondrite-normalized rare earth element
2 (REE) patterns for the same monazites.

3 Figure 9. Concordia plot (a) including all zircon with concordance >90% from sample JBP-71-15
4 (Sobrado migmatitic paragneiss), and (b) age histogram and probability density plot for ages older than
5 1000 Ma.

6 Figure 10. Tera-Wasserburg diagram (a) for the analyses between 589 and 380 Ma, and, (b) age
7 histogram and probability density plot for the same ages.

8 Figure 11. Chondrite-normalized plots for inherited zircon older than 1000 Ma.

9 Figure 12. Chondrite-normalized plots for zircon between 589 and 380 Ma.

10 Figure 13. (a) Hafnium versus age, (b) Yb/Gd versus age, (c) Eu/Eu* versus age, and (d) U/Ce versus Th
11 for zircon analyses between 589 and 380 Ma.

12 Figure 14. Th/U ratio versus $^{206}\text{Pb}/^{238}\text{U}$ ages for the zircon analyses from 589 to 380 Ma. Analysis 63
13 (510 Ma) is not represented as it has an anomalous value (6.59).

14 Figure 15. Weighted average obtained from magmatic ages distributed between 589 and 510 Ma.

15 Figure 16. Age of the onset of the oldest HP-HT metamorphic event obtained using the TuffZirc
16 algorythm.

17

18 Table 1: U-Th_Pb+REE Titanite_McD_S

19 Table 2A: U-Th_Pb+REE Monazite_McD_S

20 Table 3: U-Th_Pb Zircon sorted by age

21 Table 4A: REE Zircon_McD_S sorted by age

22 Table 4B: REE Zircon_McD_S sorted by age

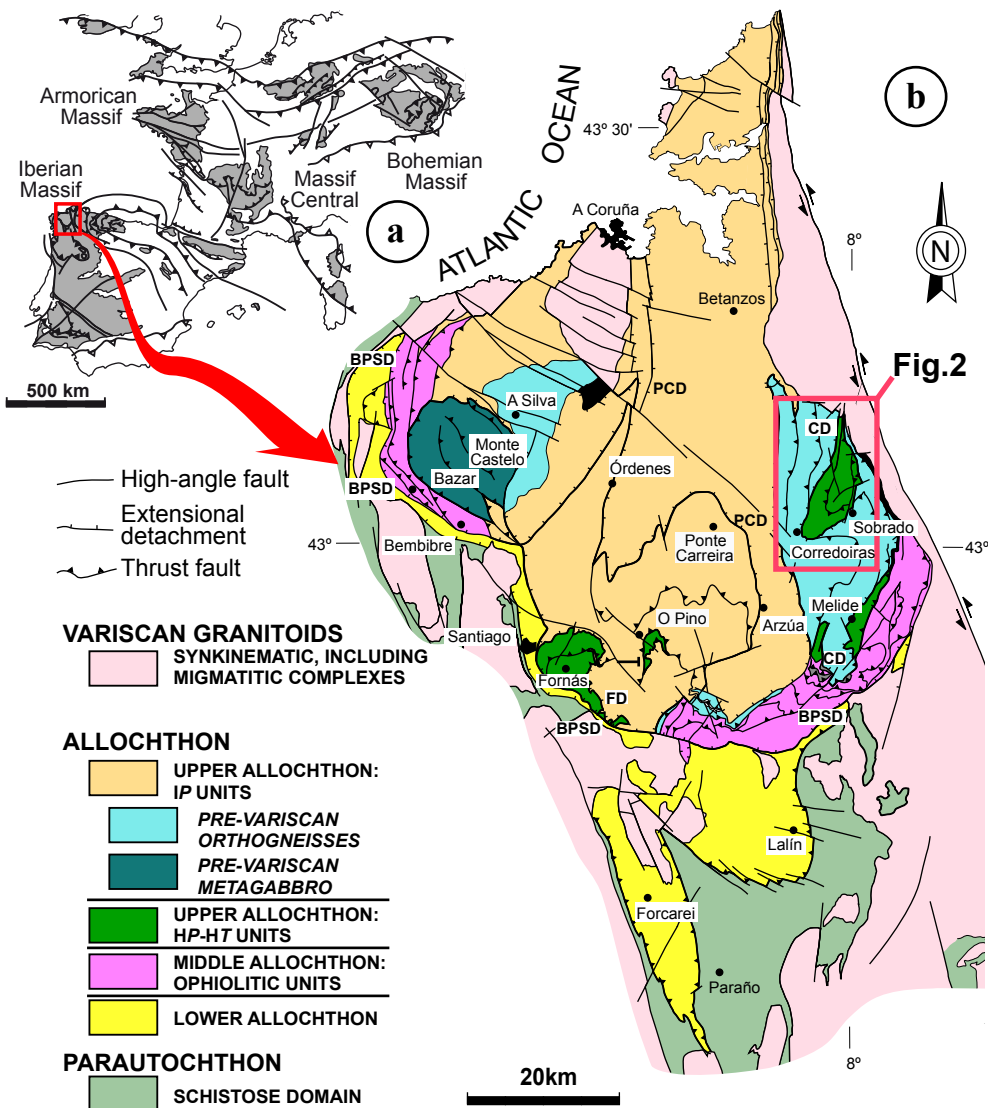


Figure 1: a) Simplified map of the Variscan orogen in Europe with the location of the Órdenes Complex. b) Map of the Órdenes Complex with indication of the main units and tectonic contacts. Extensional detachments are labeled: BPSD, Bembibre-Pico Sacro system; CD: Corredoiras; FD, Fornás; PCD, Ponte Carreira. Fig. 2 location indicated.

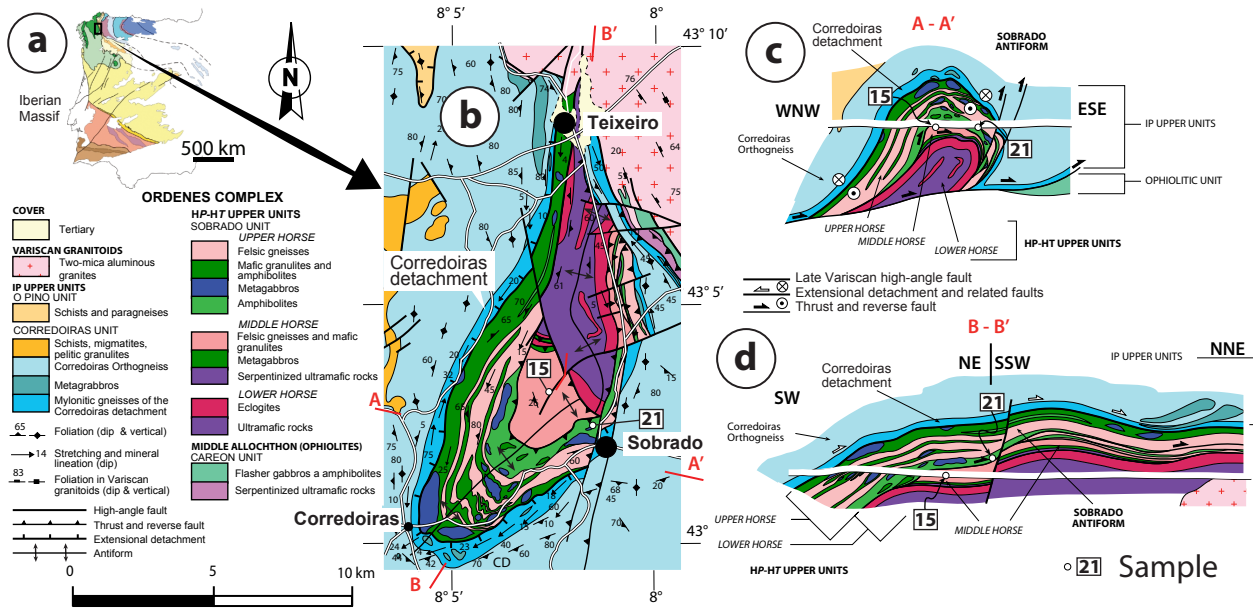


Figure 2. Geological map of the study area and location of the samples, modified from Arenas and Martínez Catalán (2002): (a) Location of the Ordenes complex within the Iberian massif. (b) Sobrado Unit map, indicating units and horses. (c) Cross-section in WNW-ESE direction and (d) SW-NE and SSW-NNE direction of the Sobrado antiform. Sample location are indicated.

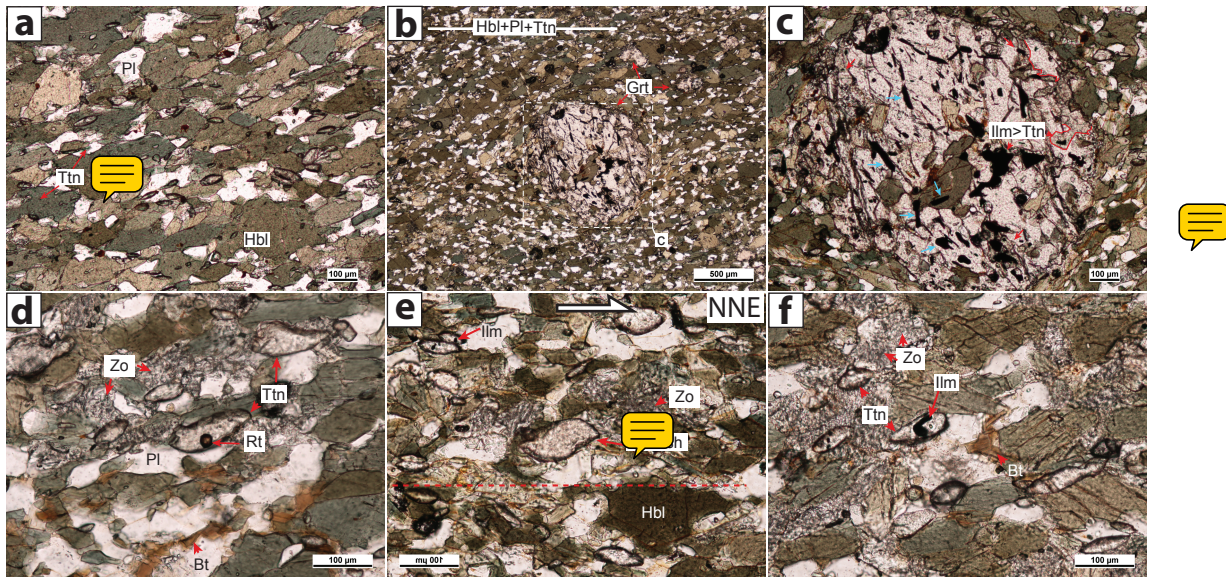


Figure 3. Fine grained amphibolites (sample JBP-71-21) from the basal mylonitic band in the Sobrado Upper horse. (a) Hornblende-plagioclase mixtures and titanite with preferred orientation, defining the mylonitic fabric. (b) Main fabric surrounding a garnet porphyroblast. Note titanite is the Ti phase in the mylonitic fabric but ilmenite grains have been preserved inside the garnet. The position of (c) is indicated by a white dashed square. (c) Garnet inclusions from (b) where ilmenite inclusions show a progressive breakdown into titanite ($\text{Ilm} > \text{Ttn}$). Note ilmenite inclusions inside pristine garnet areas show no evidence of transformation. (d) Inclusions of rutile inside titanite and partial transformation of plagioclase into zoisite. (e) Titanite mineral fish showing a top-to-the NNE shear sense. Small ilmenite inclusions are visible in titanite. (f) Retrogression of plagioclase into zoisite and ilmenite inclusions inside titanite grains parallel to the main foliation. All micrographs in plane-polarized light (PPL). (Mineral abbreviations after Whitney and Evans, 2010; Hbl: hornblende, Ttn: titanite, Ilm: ilmenite, Rt: rutile, Pl: plagioclase, Zo: zoisite, Grt: garnet).

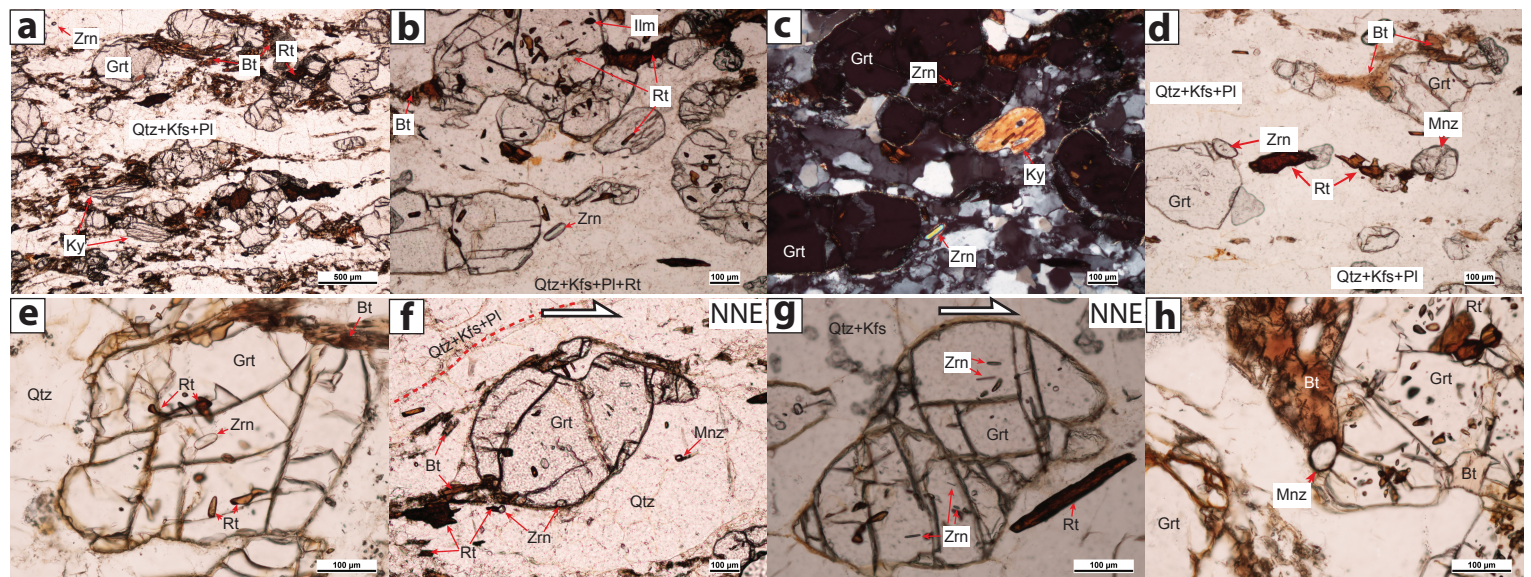


Figure 4. Granulite facies migmatitic paragneiss from the Sobrado Middle horse (Fig. 2). (a) General microstructure where leucosome bands and preferred orientation of elongated garnets, biotite, rutile and kyanite define the foliation. (b) Zircon elongated grain in recrystallized leucosome domain. Main inclusions in garnet include rutile, ilmenite and zircon (PPL) and (c) Cross-polarized light (CPL). (d) Monazite and zircon surrounded grain in the leucosome domain. (e) Subrounded elongated grain of zircon included in a garnet. (f) Plastically deformed garnet (sigmoidal grain) in a leucosome. Zircon and monazite are found in the quartz-rich area around the garnet. (g) Sigmoidal garnet in a leucosome. Inclusions of prismatic and bipiramidal zircons and rutile are observed. (h) Monazite grain in a garnet pressure shadow with biotite. Ky: kyanite, Bt: biotite, Qtz: quartz, Kfs: K-feldspar, Pl: plagioclase, Rt: rutile, Zrn: zircon, Grt: garnet.

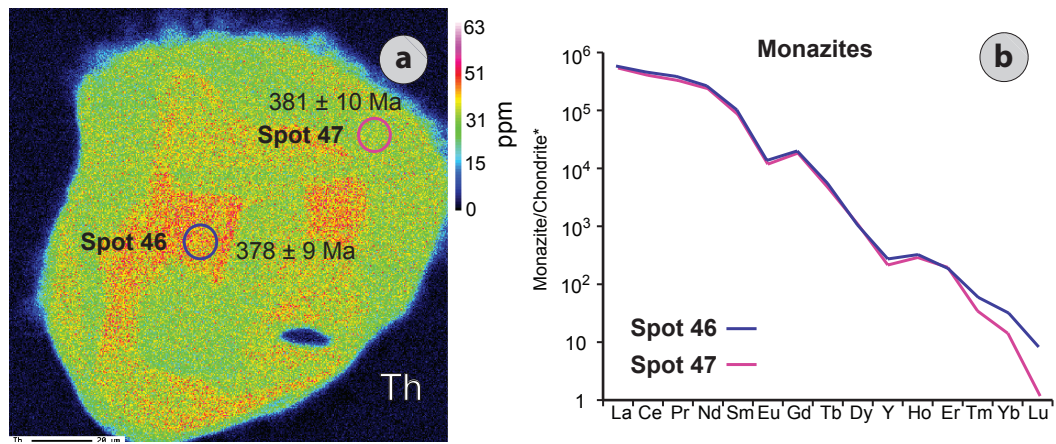


Figure 5. (a) Monazite grain compositional maps in paragneiss with a 30% thorium variation. Location and spot numbers (46 and 47) are indicated, as well as the $^{206}\text{Pb}/^{238}\text{U}$ age and error ($\pm 2\sigma$). (b) Chondrite-normalized rare earth element (REE) patterns for the same monazites in (a).

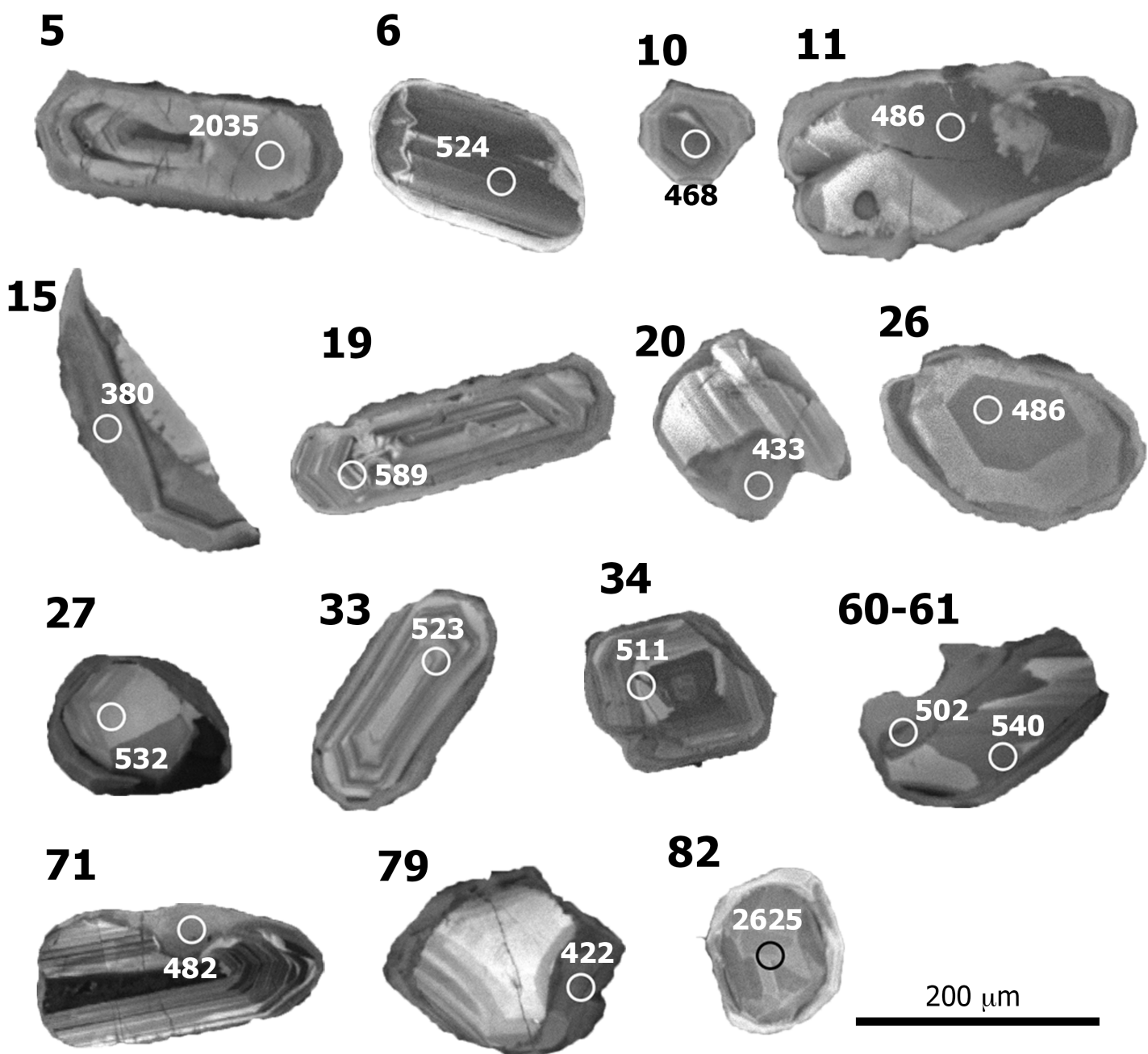


Figure 6: Cathodoluminescence (CL) images with the location of the analyzed spots for selected zircon grains.

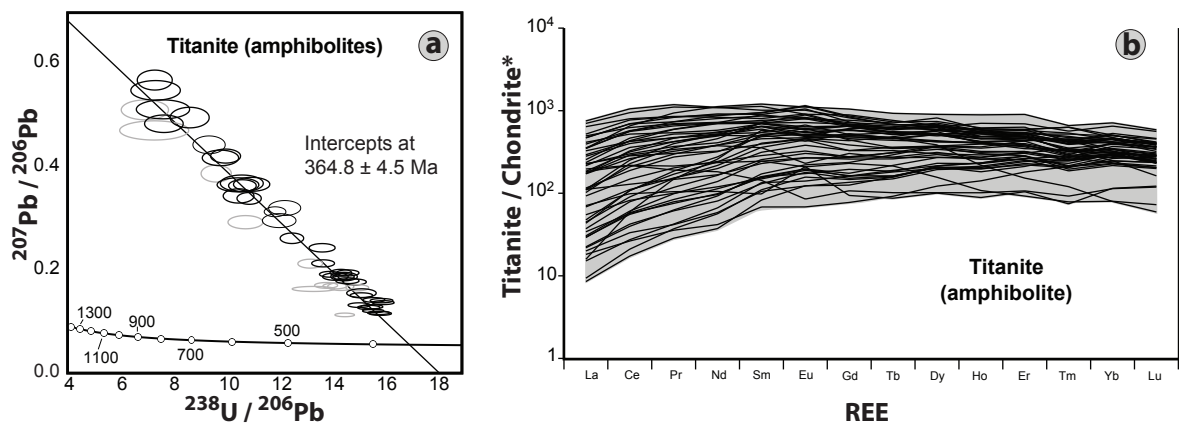


Figure 7. (a) Tera-Wasserburg diagram showing distribution of analyzed titanites ($n = 51$) from Sobrado amphibolite (JBP-71-21). The rejected analyses are represented by gray ellipses. The ellipses represent the $^{207}\text{Pb}/^{206}\text{Pb}$ and $^{238}\text{U}/^{206}\text{Pb}$ errors ($\pm 2\sigma$). (b) Chondrite-normalized rare earth element (REE) patterns for the same titanites.

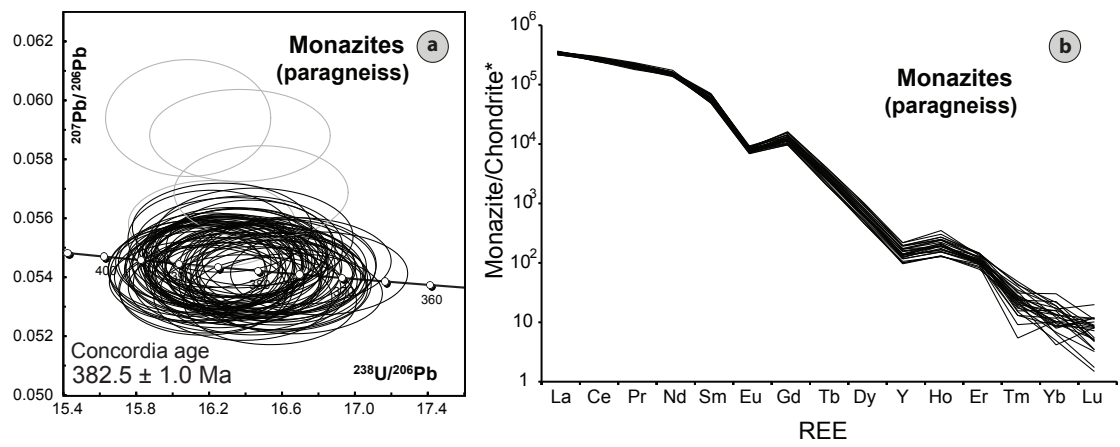


Figure 8. (a) Tera-Wasserburg diagram showing distribution of analyzed monazites ($n = 76$) from Sobrado paragneiss (JBP-71-15). The rejected analyses are represented by gray ellipses. The ellipses represent the $^{207}\text{Pb}/^{206}\text{Pb}$ and $^{238}\text{U}/^{206}\text{Pb}$ errors ($\pm 2\sigma$). (b) Chondrite-normalized rare earth element (REE) patterns for the same monazites.

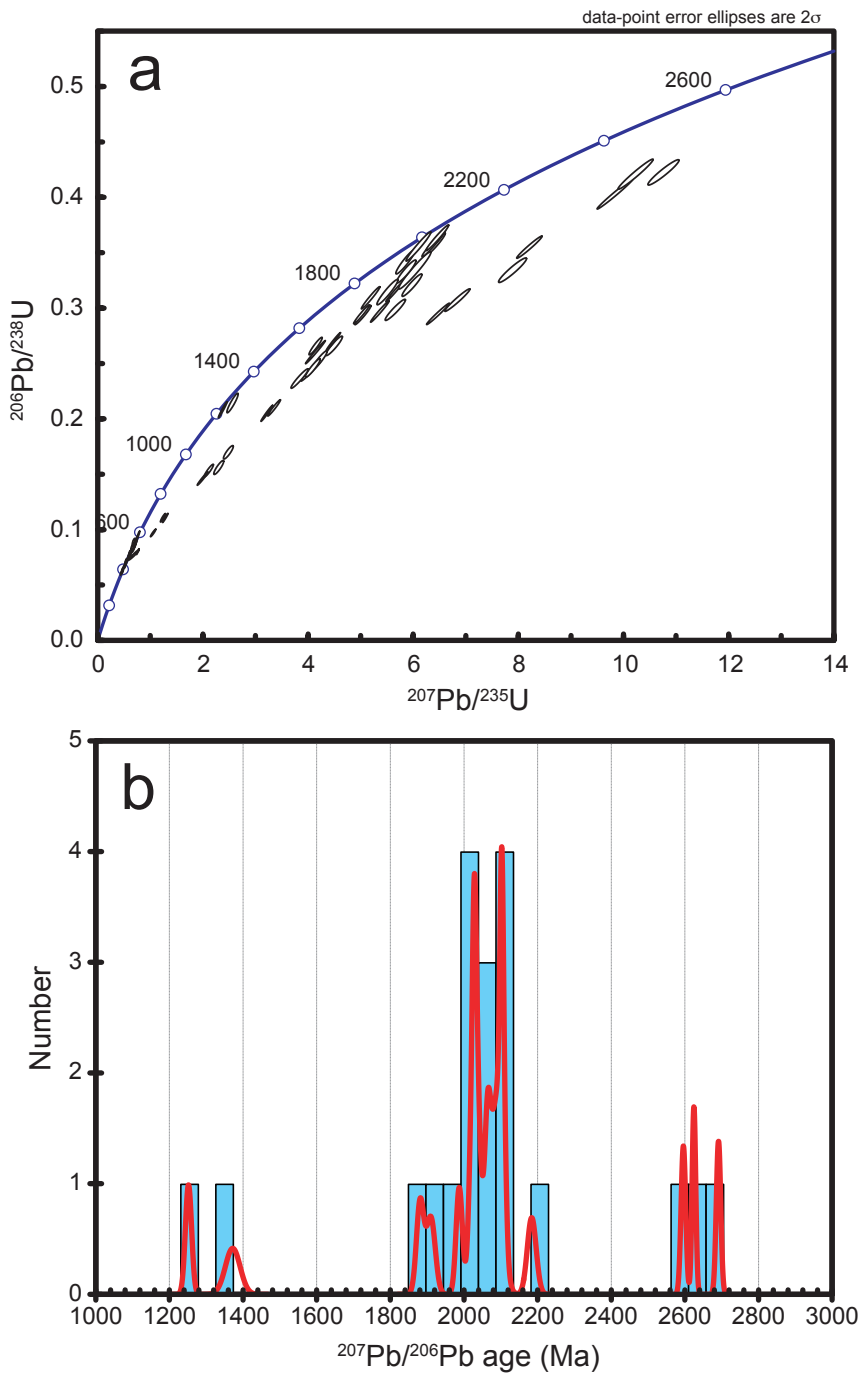


Figure 9: Concordia plot (a) including all zircon with concordance $>90\%$ from sample JBP-71-15 (Sobrado migmatitic paragneiss), and (b) age histogram and probability density plot for ages older than 1000 Ma.

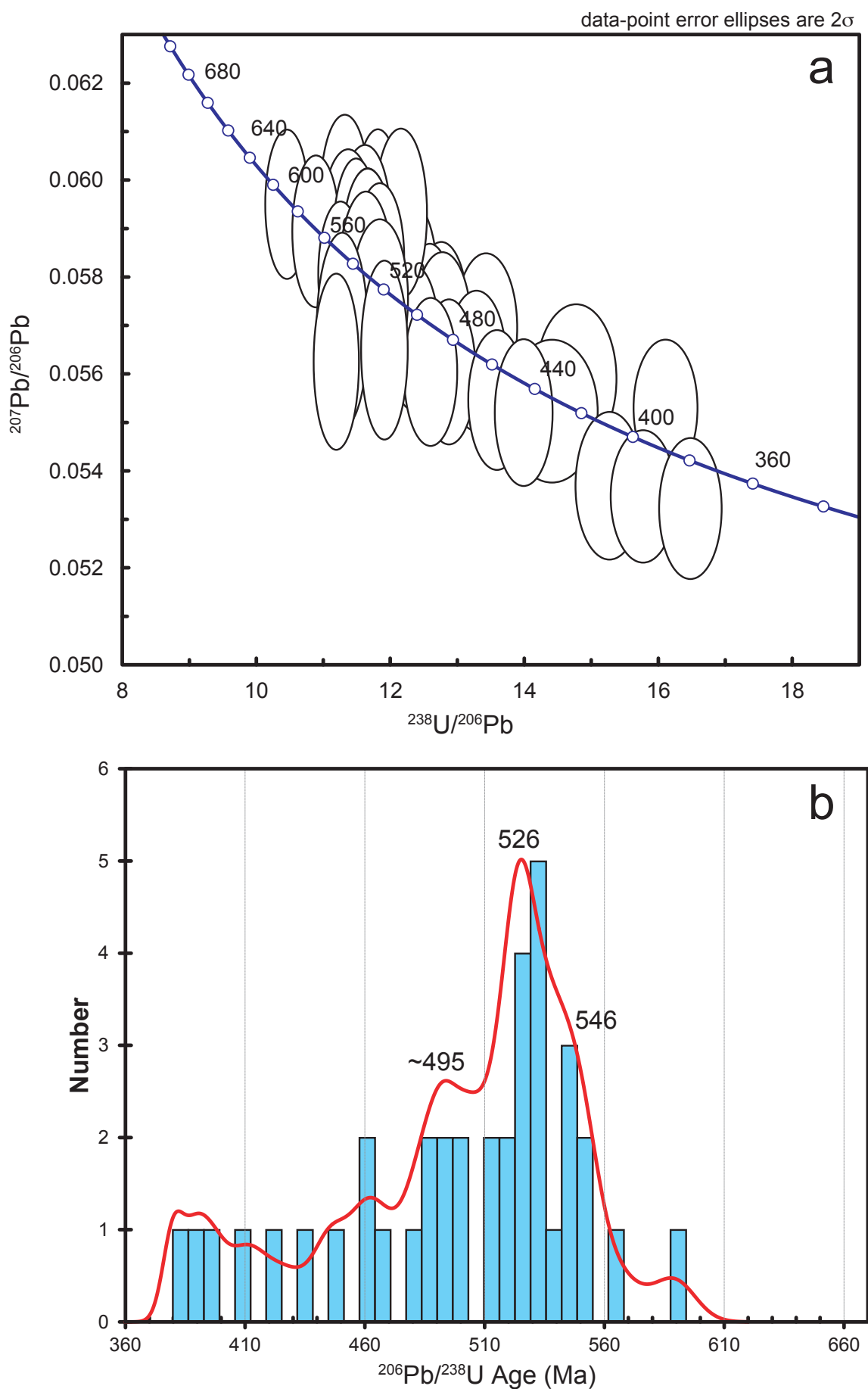


Figure 10: Tera-Wasserburg diagram (a) for the analyses between 589 and 380 Ma, and, (b) age histogram and probability density plot for the same ages.

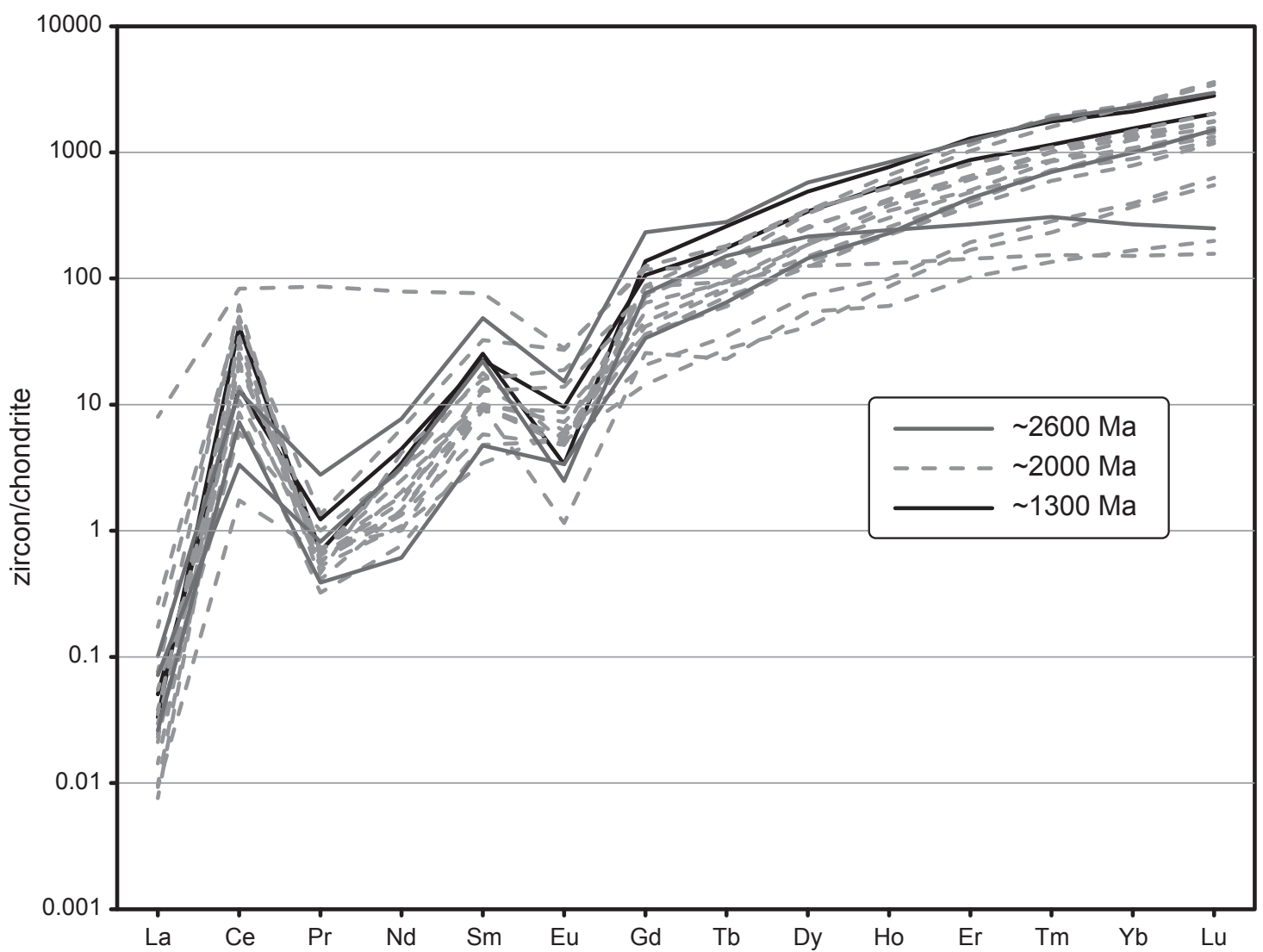


Figure 11: Chondrite-normalized plots for inherited zircon older than 1000 Ma.

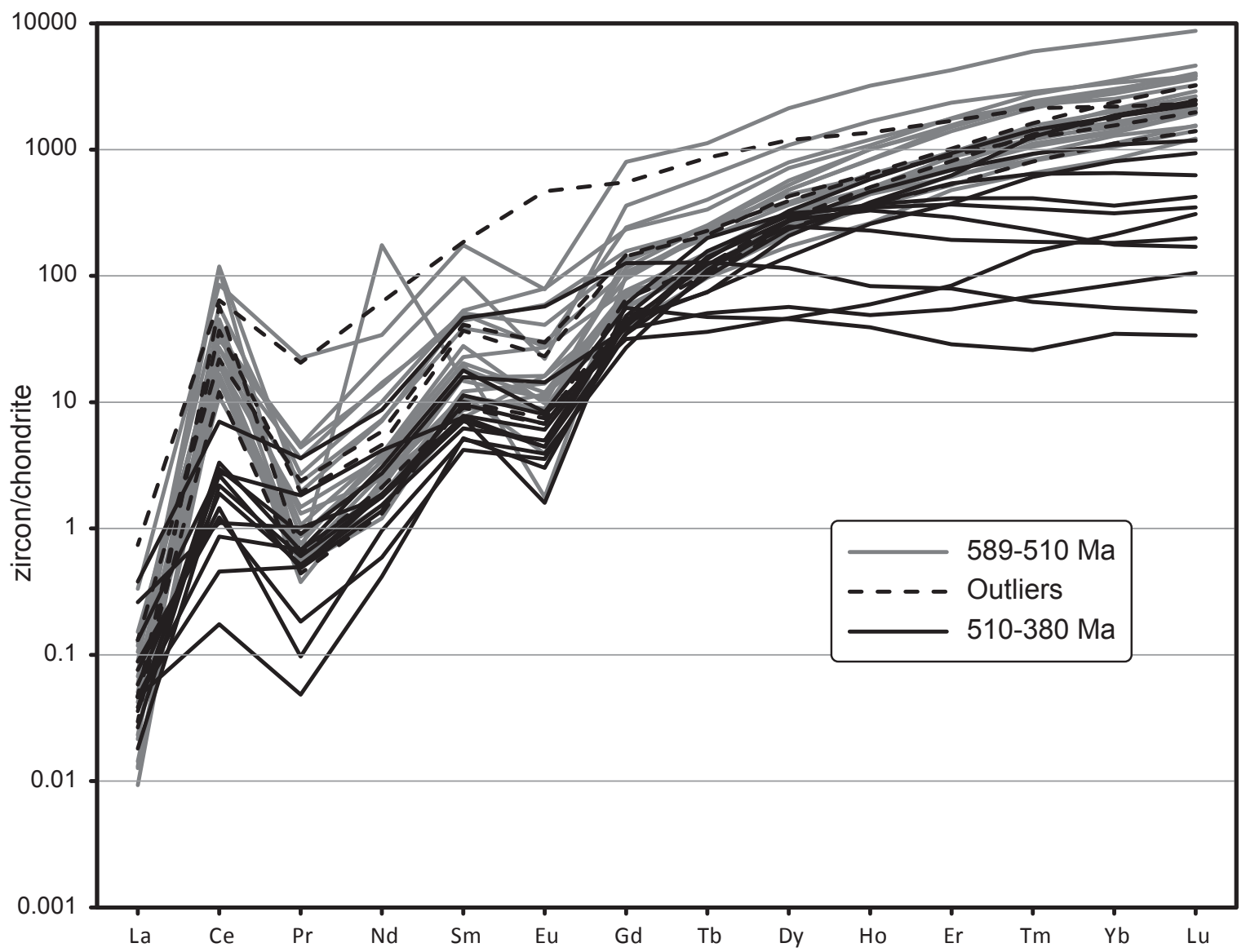


Figure 12: Chondrite-normalized plots for zircon between 589 and 380 Ma.

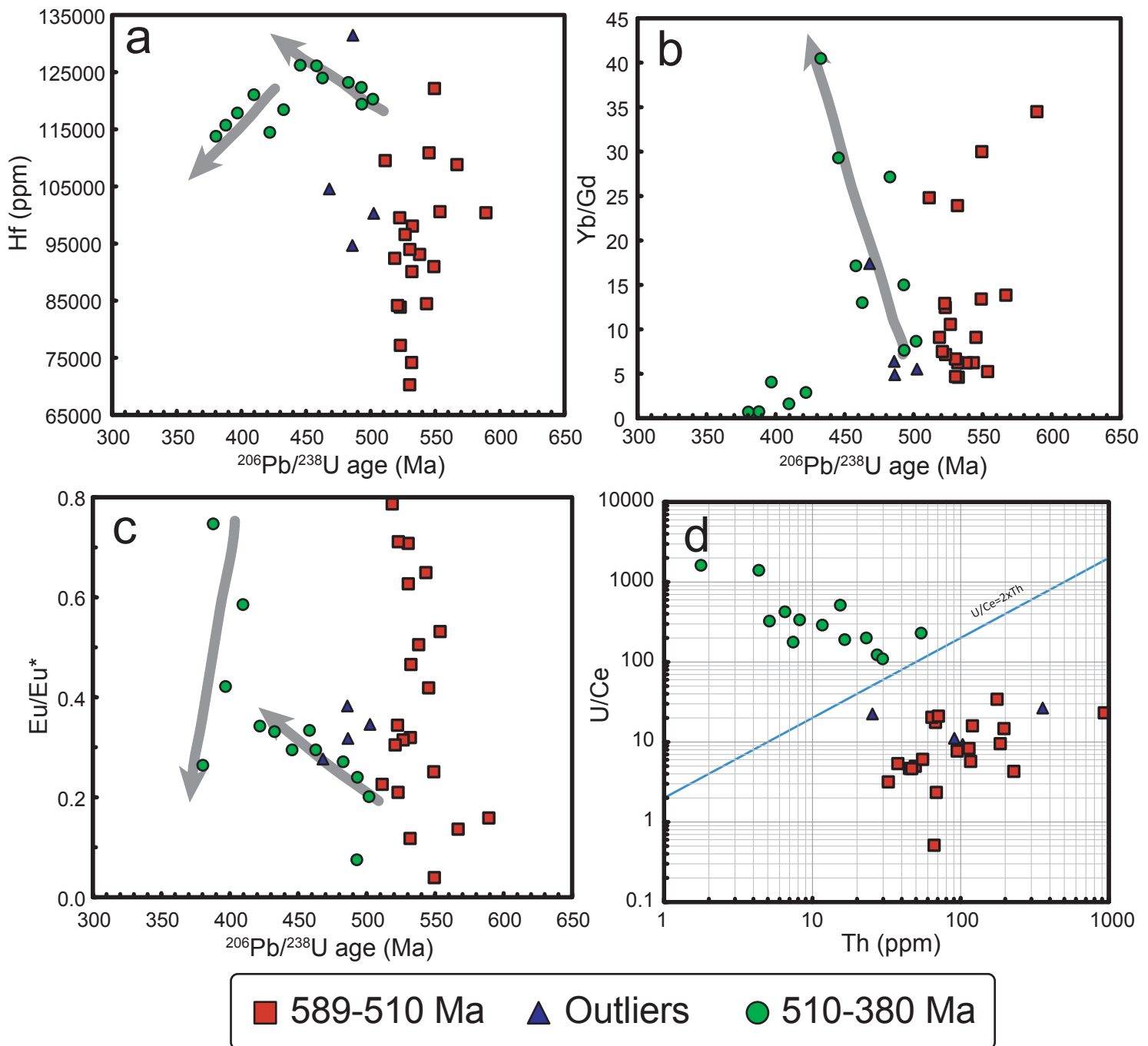


Figure 13: (a) Hafnium versus age, (b) Yb/Gd versus age, (c) Eu/Eu* versus age, and (d) U/Ce versus Th for zircon analyses between 589 and 380 Ma.

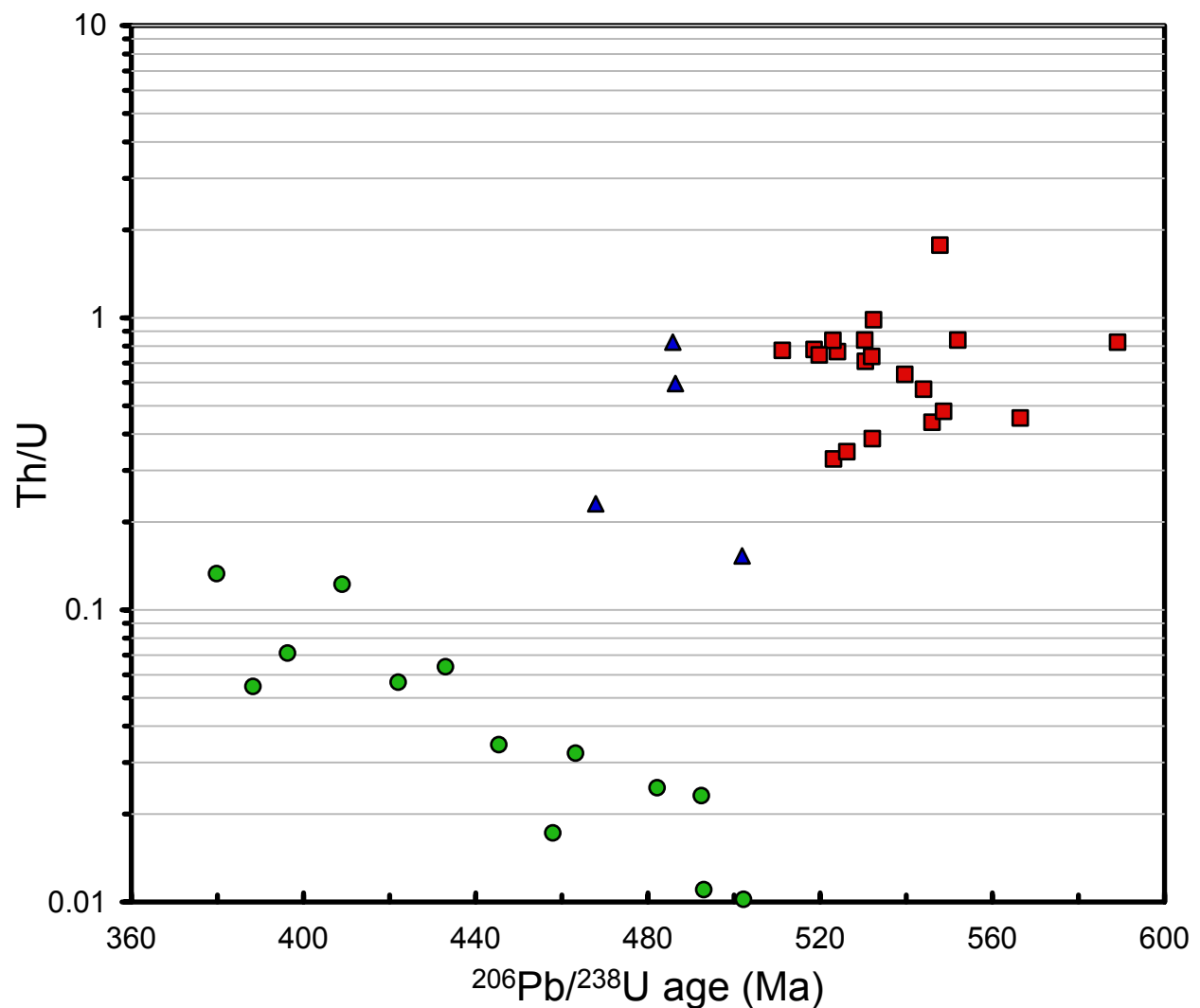


Figure 14: Th/U ratio versus $^{206}\text{Pb}/^{238}\text{U}$ ages for the zircon analyses from 589 to 380 Ma. Analysis 63 (510 Ma) is not represented as it has an anomalous value (6.59).

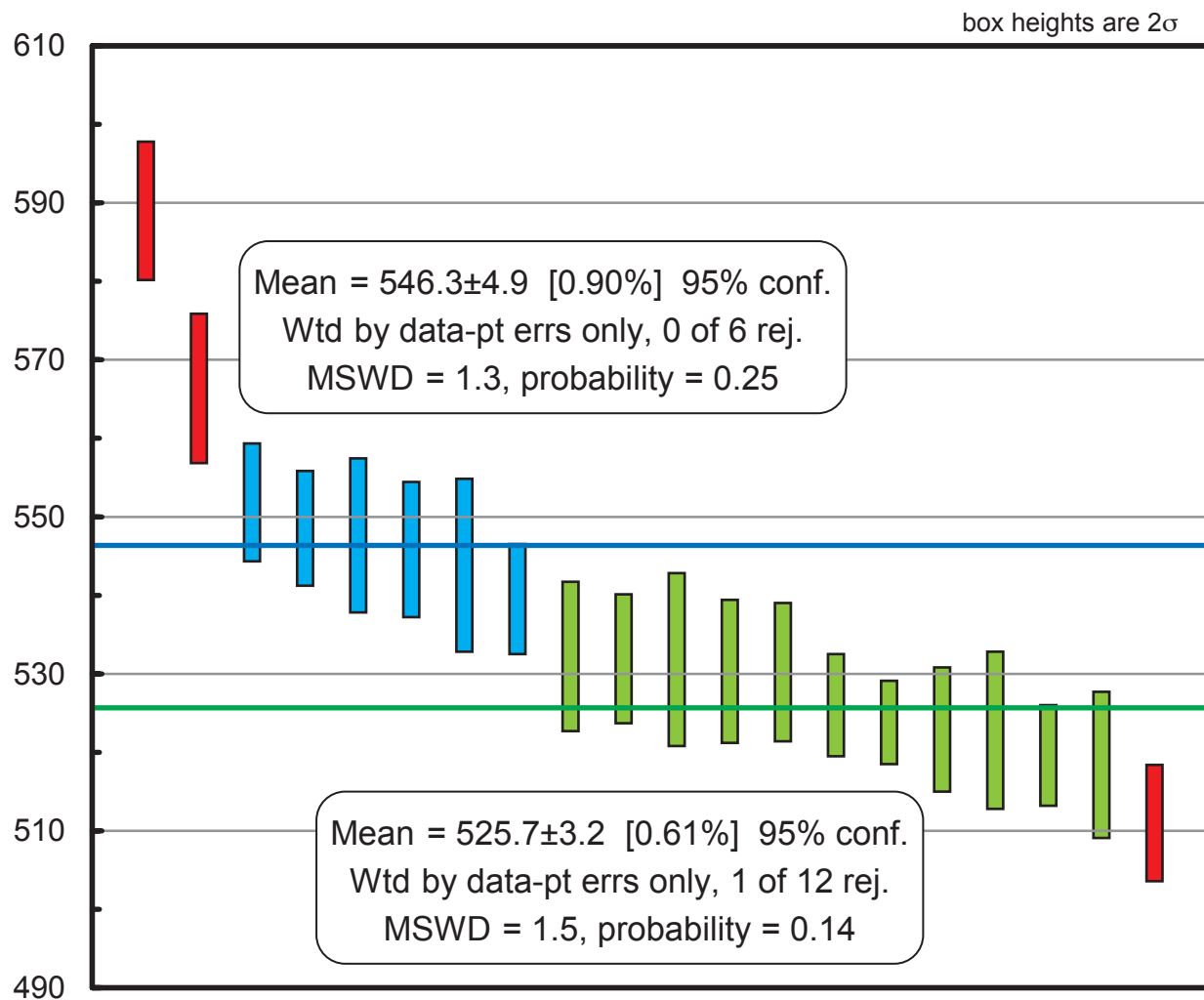


Figure 15: Weighted average obtained from magmatic ages distributed between 589 and 510 Ma.

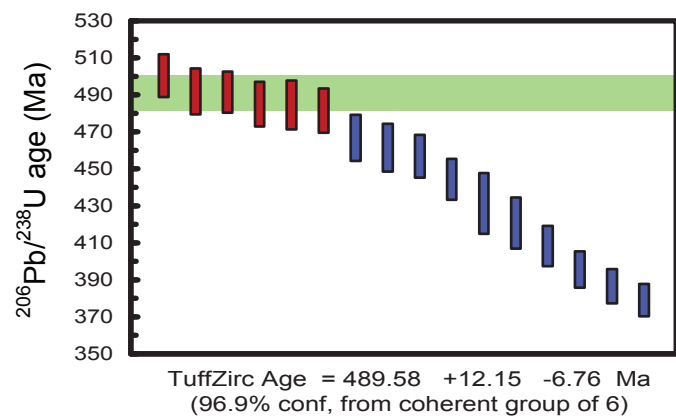


Figure 16: Age of the onset of the oldest HP-HT metamorphic event obtained using the TuffZirc algorythm.

Table 1_U-Th_Pb+REE Titatine_McD_s

Spot	$^{238}\text{U}/^{206}\text{Pb}$	$^{207}\text{Pb}/^{206}\text{Pb}$	$^{208}\text{Pb}/^{232}\text{Th}$	U (ppm)	Th (ppm)	La (ppm)	Ce (ppm)	Pr (ppm)	Nd (ppm)	Sm (ppm)	Eu (ppm)	Gd (ppm)	Tb (ppm)	Dy (ppm)	Ho (ppm)	Er (ppm)	Tm (ppm)	Yb (ppm)	Lu (ppm)
1	15.59 ± 0.35	0.1279 ± 0.0032	0.02392 ± 0.00053	7.42	16.57	751	1052	1182	1096	1012	818	681	635	590	521	423.1	405	363.4	
2	13.37 ± 0.66	0.1625 ± 0.0040	0.02580 ± 0.00074	8.22	16.73	701	946	1107	1085	1128	889	762	661	584	483	333.6	324.5	232.9	
3	13.74 ± 0.36	0.2123 ± 0.0056	0.03513 ± 0.00101	4.16	7.44	327	424	520	538	650	588	574	559	522	538	411.7	465	392.7	
4	13.85 ± 0.36	0.1694 ± 0.0046	0.05140 ± 0.00288	4.30	2.47	116	188	275	318	484	519	503	471	419	408	365	278.9	299	230.5
5	13.70 ± 0.41	0.2426 ± 0.0067	0.05450 ± 0.00376	2.71	2.35	109	209	297	383	511	458	437	422	416	386	287.9	315	261.4	
6	14.20 ± 0.40	0.1864 ± 0.0058	0.03180 ± 0.00119	3.16	4.74	225	300	369	409	547	671	515	539	495	526	511	393.5	448	383.7
7	12.06 ± 0.52	0.2955 ± 0.0111	0.15000 ± 0.01802	2.00	1.46	68	111	153	199	314	382	329	361	394	399	318.6	340	290.7	
8	14.52 ± 0.33	0.1863 ± 0.0050	0.03051 ± 0.00091	4.86	7.93	394	574	681	705	762	813	685	648	589	608	436.8	504	417.1	
9	15.11 ± 0.35	0.1310 ± 0.0037	0.02719 ± 0.00074	6.55	10.39	471	692	733	803	861	828	714	679	636	703	693	565.6	650	561.0
10	12.55 ± 0.37	0.2611 ± 0.0083	0.14400 ± 0.00410	2.35	0.96	45	90	152	217	359	442	328	329	300	291	304	252.6	290	245.5
11	15.48 ± 0.35	0.1284 ± 0.0034	0.03340 ± 0.00137	8.13	6.22	350	654	938	1120	1201	1045	928	902	890	901	659.9	711	586.6	
12	7.30 ± 1.08	0.4710 ± 0.0153	0.07200 ± 0.00961	0.61	0.32	15	27	42	67	134	140	162	189	215	233	264	248.2	287	232.1
13	10.02 ± 0.47	0.4211 ± 0.0111	0.11200 ± 0.00503	1.20	0.69	31	61	98	139	244	209	230	214	156	108	93	78.5	80	72.8
14	9.66 ± 0.47	0.3870 ± 0.0135	0.22000 ± 0.01706	1.09	0.56	29	55	79	96	159	197	160	181	200	213	249	230.4	296	242.7
15	13.99 ± 0.32	0.1910 ± 0.0046	0.03377 ± 0.00107	4.58	6.10	184	317	421	512	599	485	518	467	433	401	374	319.8	306	236.2
16	14.41 ± 0.41	0.1672 ± 0.0063	0.03150 ± 0.00144	4.02	5.44	216	359	421	492	642	501	609	590	549	545	471.3	464	395.9	
17	14.94 ± 0.36	0.1761 ± 0.0048	0.13000 ± 0.03669	4.38	0.71	43	108	170	239	404	460	433	485	572	540	536	488.3	420	339.0
18	7.35 ± 0.77	0.5490 ± 0.0155	-0.08000 ± -0.14001	0.55	0.30	18	26	36	42	68	68	77	92	122	141	181	210.9	230	204.5
19	15.96 ± 0.36	0.1397 ± 0.0034	0.02710 ± 0.00071	8.10	9.22	414	520	541	580	692	609	652	624	708	579	591	630.8	507	405.7
20	15.04 ± 0.36	0.1649 ± 0.0049	0.03031 ± 0.00096	6.39	8.79	293	426	468	522	543	499	482	455	514	419	438	446.6	412	321.1
21	11.90 ± 0.34	0.3127 ± 0.0079	0.37000 ± 0.022012	2.91	0.40	48	108	185	276	507	426	527	465	385	218	153	120.2	80	59.3
22	14.41 ± 0.34	0.1940 ± 0.0054	0.05140 ± 0.00216	5.29	3.73	255	465	598	716	889	794	766	709	817	603	595	629.1	472	382.1
23	14.18 ± 0.37	0.1682 ± 0.0046	0.09800 ± 0.00162	4.77	1.43	102	228	355	458	710	718	687	604	671	488	476	449.4	344	258.5
24	15.92 ± 0.35	0.1147 ± 0.0030	0.02888 ± 0.00057	10.78	13.20	468	695	829	915	901	1052	731	604	620	458	442	428.3	323	278.0
25	7.63 ± 0.83	0.5120 ± 0.0150	-0.03000 ± -0.49000	0.68	0.14	9	21	37	56	110	157	147	157	209	182	211	270.4	234	214.2
26	12.27 ± 0.50	0.3200 ± 0.0119	0.05770 ± 0.00542	1.68	2.17	93	148	203	243	286	325	275	274	313	271	307	349.0	312	285.4
27	14.67 ± 0.35	0.1937 ± 0.0048	0.03279 ± 0.00098	4.67	6.77	354	560	653	700	703	639	652	551	557	401	347	332.8	248	162.6
28	15.20 ± 0.46	0.1543 ± 0.0069	0.03500 ± 0.00183	4.88	4.43	174	326	463	554	642	542	593	512	581	487	521	521.1	496	453.7
29	14.56 ± 0.31	0.1120 ± 0.0029	0.02158 ± 0.00049	11.71	22.45	495	625	696	722	728	886	653	584	642	562	575	536.0	444	363.0
30	10.92 ± 0.38	0.3387 ± 0.0094	0.05840 ± 0.00378	1.54	2.51	111	129	147	168	229	267	270	312	375	364	517	454	488	392.3
31	10.64 ± 0.67	0.3680 ± 0.0132	0.12200 ± 0.03409	1.07	0.81	29	58	84	114	158	173	195	184	230	228	262	283.0	270	259.3
32	9.39 ± 0.50	0.4430 ± 0.0141	-0.02000 ± -0.12000	0.90	0.58	22	42	61	81	130	179	152	162	207	205	242	246.2	289	248.8
33	10.49 ± 0.65	0.3651 ± 0.0111	0.09500 ± 0.00969	1.13	1.22	55	82	100	120	149	189	163	162	203	196	229	210.5	247	236.6
34	15.19 ± 0.35	0.1501 ± 0.0040	0.05840 ± 0.00163	5.56	3.48	235	434	593	696	705	801	639	537	517	454	488	390.3	419	392.2
35	14.53 ± 0.41	0.1866 ± 0.0067	0.03290 ± 0.00129	3.69	4.89	172	263	322	383	457	471	483	465	516	482	494	401.6	464	401.2
36	14.66 ± 0.36	0.1785 ± 0.0047	0.05840 ± 0.00378	4.36	2.21	111	252	399	514	703	588	649	544	524	463	461	351.8	391	368.3
37	16.03 ± 0.34	0.1359 ± 0.0032	0.04720 ± 0.00230	8.41	3.38	281	400	473	503	493	611	443	355	366	321	320	264.8	297	287.8
38	10.52 ± 0.48	0.3435 ± 0.0113	0.14400 ± 0.06906	1.28	0.55	22	40	63	93	172	221	236	293	370	352	385	304.0	348	308.1
39	8.65 ± 0.61	0.4960 ± 0.0164	0.00000 ± 0.00000	0.66	0.24	9	17	29	37	83	123	126	158	215	232	284	278	267.9	345.9
40	15.85 ± 0.34	0.1160 ± 0.0028	0.02681 ± 0.00080	7.59	7.20	348	566	735	869	950	1151	862	731	739	619	632	420.2	550	460.6
41	11.89 ± 0.31	0.1654 ± 0.0046	0.06000 ± 0.04000	0.57	0.33	20	33	42	58	105	123	136	150	193	200	221	204.0	263	280.5
42	9.82 ± 0.57	0.4175 ± 0.0124	0.03790 ± 0.00242	2.61	4.41	228	284	304	324	395	455	445	455	425	518	411	362.2	427	204.9
43	15.67 ± 0.34	0.1411 ± 0.0037	0.02576 ± 0.00068	6.21	10.38	640	799	852	832	803	913	671	607	625	520	493	319.8	397	362.2
44	11.01 ± 0.57	0.3661 ± 0.0111	0.11000 ± 0.14002	1.20	0.86	34	57	75	99	154	196	174	218	270	274	316	272.5	369	345.9
45	7.67 ± 0.60	0.4840 ± 0.0139	0.04000 ± 0.02500	0.57	0.33	20	33	42	58	105	123	136	150	193	200	221	204.0	263	280.5
46	13.25 ± 0.39	0.2117 ± 0.0071	0.03790 ± 0.00242	2.61	4.41	228	284	304	324	395	455	445	455	425	518	411	362.2	427	204.9
47	10.78 ± 0.54	0.2924 ± 0.0124	0.03790 ± 0.00242	1.66	0.79	37	79	118	165	255	304	304	309	313	321	321	288.2	305	288.2
48	6.94 ± 0.74	0.5110 ± 0.0158	0.07450 ± 0.00745	0.64	1.89	173	290	339	376	356	303	269	273	260	255	255	186.6	217	199.2
49	15.64 ± 0.33	0.1197 ± 0.0028	0.03214 ± 0.00100	10.32	7.50	521	772	845	886	937	1130	879	683	551	478	339	292.2	345.9	299.2
50	10.66 ± 0.43	0.3635 ± 0.0094	0.06970 ± 0.00481	1.77	2.45	197	218	235	245	269	294	255	229	258	279	210.9	246	236.6	
51	7.32 ± 0.55	0.5690 ± 0.0158	0.08940 ± 0.00820	0.70	1.76	183	217	191	182	143	85	107	102	101	107	102	101	107	114

Table 2A_U-Th_Pb+REE Monazite_McD_S

Spot	$^{238}\text{U}/^{206}\text{Pb}$	$^{207}\text{Pb}/^{206}\text{Pb}$	$^{208}\text{Pb}/^{206}\text{Pb}$	$\text{U} \text{ (ppm)}$	$\text{Th} \text{ (ppm)}$	$\text{La} \text{ (ppm)}$	$\text{Ce} \text{ (ppm)}$	$\text{Pr} \text{ (ppm)}$	$\text{Nd} \text{ (ppm)}$	$\text{Sm} \text{ (ppm)}$	$\text{Eu} \text{ (ppm)}$	$\text{Gd} \text{ (ppm)}$	$\text{Tb} \text{ (ppm)}$	$\text{Dy} \text{ (ppm)}$	$\text{Y} \text{ (ppm)}$	$\text{Ho} \text{ (ppm)}$	$\text{Er} \text{ (ppm)}$	$\text{Tm} \text{ (ppm)}$	$\text{Yb} \text{ (ppm)}$	$\text{Lu} \text{ (ppm)}$
1	16.29 ± 0.35	0.0543 ± 0.00013	0.01930 ± 0.00041	1640 ± 0.00042	1850 ± 0.00042	28300 ± 0.00042	527004 ± 0.00042	437194 ± 0.00042	352371 ± 0.00042	943245 ± 0.00042	13286 ± 0.00042	19749 ± 0.00042	4490 ± 0.00042	1081 ± 0.00042	12131 ± 0.00042	19899 ± 0.00042	4429 ± 0.00042	243 ± 0.00042	324 ± 0.00042	
2	16.28 ± 0.35	0.0545 ± 0.00013	0.01916 ± 0.00042	1850 ± 0.00042	25500 ± 0.00042	519409 ± 0.00042	420881 ± 0.00042	250109 ± 0.00042	12451 ± 0.00042	90608 ± 0.00042	12451 ± 0.00042	17769 ± 0.00042	5319 ± 0.00042	1163 ± 0.00042	1282 ± 0.00042	190 ± 0.00042	374 ± 0.00042	22 ± 0.00042	25 ± 0.00042	
3	16.20 ± 0.38	0.0544 ± 0.00013	0.01949 ± 0.00042	2300 ± 0.00042	34200 ± 0.00042	5633713 ± 0.00042	425775 ± 0.00042	223632 ± 0.00042	85270 ± 0.00042	11474 ± 0.00042	18843 ± 0.00042	4266 ± 0.00042	898 ± 0.00042	192 ± 0.00042	118 ± 0.00042	466 ± 0.00042	6 ± 0.00042	122 ± 0.00042	24 ± 0.00042	
4	16.30 ± 0.38	0.0546 ± 0.00013	0.01930 ± 0.00042	1454 ± 0.00042	32400 ± 0.00042	1805 ± 0.00042	352448 ± 0.00042	420881 ± 0.00042	231947 ± 0.00042	92568 ± 0.00042	11385 ± 0.00042	959 ± 0.00042	1197 ± 0.00042	143 ± 0.00042	260 ± 0.00042	143 ± 0.00042	14 ± 0.00042	0.0 ± 0.00042	0.0 ± 0.00042	
5	16.18 ± 0.36	0.0543 ± 0.00012	0.01926 ± 0.00043	1805 ± 0.00043	34200 ± 0.00043	420881 ± 0.00043	231947 ± 0.00043	92568 ± 0.00043	11385 ± 0.00043	9899 ± 0.00043	11385 ± 0.00043	9197 ± 0.00043	11385 ± 0.00043	143 ± 0.00043	260 ± 0.00043	143 ± 0.00043	14 ± 0.00043	0.0 ± 0.00043	0.0 ± 0.00043	
6	16.09 ± 0.35	0.0546 ± 0.00012	0.01944 ± 0.00044	1860 ± 0.00044	32800 ± 0.00044	420881 ± 0.00044	231947 ± 0.00044	92568 ± 0.00044	11385 ± 0.00044	9899 ± 0.00044	11385 ± 0.00044	9197 ± 0.00044	11385 ± 0.00044	143 ± 0.00044	260 ± 0.00044	143 ± 0.00044	14 ± 0.00044	0.0 ± 0.00044	0.0 ± 0.00044	
7	16.27 ± 0.36	0.0544 ± 0.00012	0.01938 ± 0.00045	1790 ± 0.00045	29000 ± 0.00045	554430 ± 0.00045	442088 ± 0.00045	230853 ± 0.00045	95676 ± 0.00045	12847 ± 0.00045	19698 ± 0.00045	4072 ± 0.00045	1045 ± 0.00045	248 ± 0.00045	310 ± 0.00045	172 ± 0.00045	46.6 ± 0.00045	20 ± 0.00045	30.5 ± 0.00045	
8	16.15 ± 0.36	0.0545 ± 0.00012	0.01920 ± 0.00045	2170 ± 0.00045	44100 ± 0.00045	579325 ± 0.00045	437194 ± 0.00045	359914 ± 0.00045	245295 ± 0.00045	97838 ± 0.00045	13179 ± 0.00045	18893 ± 0.00045	3875 ± 0.00045	927 ± 0.00045	203 ± 0.00045	306 ± 0.00045	42.1 ± 0.00045	12 ± 0.00045	8.1 ± 0.00045	
9	16.22 ± 0.37	0.0548 ± 0.00012	0.01946 ± 0.00045	2150 ± 0.00045	47100 ± 0.00045	567511 ± 0.00045	422512 ± 0.00045	340517 ± 0.00045	245295 ± 0.00045	90608 ± 0.00045	12451 ± 0.00045	17769 ± 0.00045	3958 ± 0.00045	902 ± 0.00045	232 ± 0.00045	286 ± 0.00045	52.2 ± 0.00045	6 ± 0.00045	25.6 ± 0.00045	
10	16.38 ± 0.37	0.0549 ± 0.00012	0.01940 ± 0.00045	1650 ± 0.00045	27900 ± 0.00045	526160 ± 0.00045	435563 ± 0.00045	345759 ± 0.00045	242451 ± 0.00045	93819 ± 0.00045	12664 ± 0.00045	19799 ± 0.00045	4078 ± 0.00045	947 ± 0.00045	210 ± 0.00045	264 ± 0.00045	46.2 ± 0.00045	11 ± 0.00045	8.9 ± 0.00045	
11	16.20 ± 0.37	0.0545 ± 0.00012	0.01930 ± 0.00045	1950 ± 0.00045	30800 ± 0.00045	555274 ± 0.00045	433931 ± 0.00045	368621 ± 0.00045	254923 ± 0.00045	95270 ± 0.00045	12060 ± 0.00045	19296 ± 0.00045	4432 ± 0.00045	996 ± 0.00045	221 ± 0.00045	321 ± 0.00045	44.1 ± 0.00045	17 ± 0.00045	5.7 ± 0.00045	
12	16.29 ± 0.37	0.0546 ± 0.00012	0.01915 ± 0.00045	2280 ± 0.00045	32800 ± 0.00045	555274 ± 0.00045	431597 ± 0.00045	336207 ± 0.00045	252298 ± 0.00045	903176 ± 0.00045	13215 ± 0.00045	20201 ± 0.00045	976 ± 0.00045	236 ± 0.00045	280 ± 0.00045	195 ± 0.00045	39.7 ± 0.00045	7 ± 0.00045	0.0 ± 0.00045	
13	16.35 ± 0.38	0.0548 ± 0.00012	0.01897 ± 0.00045	2230 ± 0.00045	43200 ± 0.00045	540928 ± 0.00045	411033 ± 0.00045	349138 ± 0.00045	246827 ± 0.00045	94662 ± 0.00045	12202 ± 0.00045	18643 ± 0.00045	4551 ± 0.00045	976 ± 0.00045	218 ± 0.00045	282 ± 0.00045	138 ± 0.00045	13 ± 0.00045	0.0 ± 0.00045	
14	16.28 ± 0.36	0.0545 ± 0.00012	0.01908 ± 0.00045	2060 ± 0.00045	41000 ± 0.00045	564135 ± 0.00045	438825 ± 0.00045	362069 ± 0.00045	230197 ± 0.00045	95608 ± 0.00045	12075 ± 0.00045	19296 ± 0.00045	4269 ± 0.00045	9866 ± 0.00045	209 ± 0.00045	301 ± 0.00045	42.1 ± 0.00045	13 ± 0.00045	11.8 ± 0.00045	
15	16.31 ± 0.39	0.0545 ± 0.00012	0.01920 ± 0.00045	2020 ± 0.00045	29600 ± 0.00045	535965 ± 0.00045	420247 ± 0.00045	340517 ± 0.00045	245295 ± 0.00045	90323 ± 0.00045	13268 ± 0.00045	19032 ± 0.00045	42412 ± 0.00045	975 ± 0.00045	232 ± 0.00045	286 ± 0.00045	52.2 ± 0.00045	6 ± 0.00045	8.1 ± 0.00045	
16	16.23 ± 0.36	0.0544 ± 0.00012	0.01953 ± 0.00045	1714 ± 0.00045	31400 ± 0.00045	562447 ± 0.00045	426033 ± 0.00045	391164 ± 0.00045	261050 ± 0.00045	103514 ± 0.00045	13748 ± 0.00045	19196 ± 0.00045	4432 ± 0.00045	988 ± 0.00045	214 ± 0.00045	244 ± 0.00045	43.2 ± 0.00045	14 ± 0.00045	12.2 ± 0.00045	
17	16.40 ± 0.37	0.0547 ± 0.00012	0.01930 ± 0.00045	1950 ± 0.00045	30800 ± 0.00045	555274 ± 0.00045	433931 ± 0.00045	366379 ± 0.00045	241357 ± 0.00045	966889 ± 0.00045	12398 ± 0.00045	18894 ± 0.00045	4432 ± 0.00045	996 ± 0.00045	221 ± 0.00045	288 ± 0.00045	44.1 ± 0.00045	17 ± 0.00045	5.7 ± 0.00045	
18	16.22 ± 0.36	0.0545 ± 0.00012	0.01943 ± 0.00045	1862 ± 0.00045	30800 ± 0.00045	565051 ± 0.00045	449429 ± 0.00045	376078 ± 0.00045	262363 ± 0.00045	100000 ± 0.00045	12247 ± 0.00045	18894 ± 0.00045	4654 ± 0.00045	1081 ± 0.00045	228 ± 0.00045	308 ± 0.00045	48.2 ± 0.00045	17 ± 0.00045	8.9 ± 0.00045	
19	16.25 ± 0.38	0.0538 ± 0.00012	0.01932 ± 0.00045	1600 ± 0.00045	31200 ± 0.00045	5618143 ± 0.00045	4424420 ± 0.00045	3440288 ± 0.00045	244420 ± 0.00045	101419 ± 0.00045	12593 ± 0.00045	18643 ± 0.00045	4399 ± 0.00045	102050 ± 0.00045	2050 ± 0.00045	34.0 ± 0.00045	161 ± 0.00045	4.8 ± 0.00045		
20	16.11 ± 0.35	0.0545 ± 0.00012	0.01915 ± 0.00045	2190 ± 0.00045	34200 ± 0.00045	567932 ± 0.00045	427406 ± 0.00045	363204 ± 0.00045	2430919 ± 0.00045	9740919 ± 0.00045	12611 ± 0.00045	19899 ± 0.00045	4598 ± 0.00045	101351 ± 0.00045	209 ± 0.00045	301 ± 0.00045	30.8 ± 0.00045	13 ± 0.00045	11.8 ± 0.00045	
21	16.17 ± 0.35	0.0543 ± 0.00012	0.01920 ± 0.00045	1804 ± 0.00045	28900 ± 0.00045	537975 ± 0.00045	443719 ± 0.00045	363302 ± 0.00045	243326 ± 0.00045	109608 ± 0.00045	13248 ± 0.00045	18693 ± 0.00045	4197 ± 0.00045	1051 ± 0.00045	208 ± 0.00045	306 ± 0.00045	39.7 ± 0.00045	17 ± 0.00045	3.3 ± 0.00045	
22	16.08 ± 0.35	0.0543 ± 0.00012	0.01964 ± 0.00045	2380 ± 0.00045	32800 ± 0.00045	560338 ± 0.00045	4486113 ± 0.00045	388621 ± 0.00045	249672 ± 0.00045	101554 ± 0.00045	12913 ± 0.00045	19497 ± 0.00045	4432 ± 0.00045	1065 ± 0.00045	222 ± 0.00045	308 ± 0.00045	56.7 ± 0.00045	16 ± 0.00045	9.3 ± 0.00045	
23	16.08 ± 0.35	0.0538 ± 0.00012	0.01886 ± 0.00045	1704 ± 0.00045	34200 ± 0.00045	584000 ± 0.00045	442044 ± 0.00045	385776 ± 0.00045	231947 ± 0.00045	87635 ± 0.00045	12487 ± 0.00045	18681 ± 0.00045	4287 ± 0.00045	10191 ± 0.00045	228 ± 0.00045	308 ± 0.00045	40.7 ± 0.00045	16 ± 0.00045	10.7 ± 0.00045	
24	16.18 ± 0.39	0.0536 ± 0.00012	0.01912 ± 0.00045	1650 ± 0.00045	29500 ± 0.00045	561772 ± 0.00045	417618 ± 0.00045	352931 ± 0.00045	241517 ± 0.00045	101551 ± 0.00045	12813 ± 0.00045	19497 ± 0.00045	44247 ± 0.00045	10209 ± 0.00045	229 ± 0.00045	308 ± 0.00045	40.7 ± 0.00045	16 ± 0.00045	10.7 ± 0.00045	
25	16.37 ± 0.39	0.0546 ± 0.00012	0.01876 ± 0.00045	1900 ± 0.00045	37800 ± 0.00045	564557 ± 0.00045	417618 ± 0.00045	323604 ± 0.00045	2423545 ± 0.00045	973635 ± 0.00045	12700 ± 0.00045	19488 ± 0.00045	4488 ± 0.00045	10637 ± 0.00045	228 ± 0.00045	308 ± 0.00045	56.3 ± 0.00045	16 ± 0.00045	14.6 ± 0.00045	
26	16.43 ± 0.38	0.0540 ± 0.00012	0.01934 ± 0.00045	2130 ± 0.00045	29500 ± 0.00045	566667 ± 0.00045	422512 ± 0.00045	363502 ± 0.00045	249453 ± 0.00045	102703 ± 0.00045	13144 ± 0.00045	19140 ± 0.00045	4483 ± 0.00045	10347 ± 0.00045	228 ± 0.00045	308 ± 0.00045	39.7 ± 0.00045	17 ± 0.00045	7.3 ± 0.00045	
27	16.32 ± 0.37	0.0541 ± 0.00012	0.01944 ± 0.00045	1950 ± 0.00045	30300 ± 0.00045	567975 ± 0.00045	437199 ± 0.00045	363302 ± 0.00045	243326 ± 0.00045	102687 ± 0.00045	13197 ± 0.00045	190638 ± 0.00045	4177 ± 0.00045	10347 ± 0.00045	228 ± 0.00045	308 ± 0.00045	45.7 ± 0.00045	16 ± 0.00045	16.7 ± 0.00045	
28	16.35 ± 0.38	0.0544 ± 0.00012	0.01944 ± 0.00045	1950 ± 0.00045	30800 ± 0.00045	562700 ± 0.00045	445351 ± 0.00045	363147 ± 0.00045	246770 ± 0.00045	1018243 ± 0.00045	12824 ± 0.00045	19648 ± 0.00045	4498 ± 0.00045	1053 ± 0.00045	228					

Table 2B_U-Th_Pb+REE Monazite _ McD_S

Spot	^{238}U	^{206}Pb	^{207}Pb	^{208}Pb	^{232}Th	U (ppm)	Th (ppm)	La (ppm)	Ce (ppm)	Pr (ppm)	Nd (ppm)	Sm (ppm)	Eu (ppm)	Gd (ppm)	Tb (ppm)	Dy (ppm)	Y (ppm)	Ho (ppm)	Er (ppm)	Tm (ppm)	Lu (ppm)	Yb (ppm)	
50	16.40	± 0.37	0.0543	± 0.0012	0.01944	± 0.00045	2020	316100	561603	411093	340517	233479	92338	12131	19196	4598	1000	219	337	168	21.5	14	16.7
51	16.66	± 0.40	0.0534	± 0.0011	0.01944	± 0.00047	4730	33200	523207	432300	303819	243545	110135	14512	23879	6759	1650	358	575	217	79.8	31	7.7
52	16.54	± 0.40	0.0540	± 0.00122	0.01953	± 0.000489	1900	36500	5836654	359914	474715	288425	111283.8	14547	21859	5983	1341	318	410	239	69.6	35.4	13.4
53	16.61	± 0.42	0.0544	± 0.00132	0.01891	± 0.000502	1596	66200	545992	412398	295259	233260	84932.43	11758	18593	4391	1085	255	308	212	30.0	11.2	5.3
54	16.49	± 0.39	0.0569	± 0.00129	0.01916	± 0.000475	1611	57800	542616	437194	352371	244201	100202.7	13499	20804	4931	1084	232	350	159	36.4	21.7	8.1
55	16.34	± 0.48	0.0537	± 0.00125	0.01950	± 0.000545	1760	30200	581013	476346	371767	246827	94729.73	13357	19899	4377	1024	193	251	169	32.8	25.5	5.7
56	16.80	± 0.40	0.0541	± 0.00115	0.01912	± 0.000446	2240	37600	536709	438825	33529	235449	84797.3	11758	16985	4177	996	204	288	164	40.9	28.6	8.1
57	16.49	± 0.41	0.0540	± 0.00113	0.01979	± 0.000522	3610	30800	526160	461664	355603	247484	111621.6	13979	26533	6648	1602	318	447	240	51.0	49.7	18.3
58	16.33	± 0.40	0.0544	± 0.00121	0.0196	± 0.000471	2110	39100	566354	464927	329741	240700	80000	11279	16030	3767	748	165	216	128	38.9	16.8	0.0
59	16.59	± 0.38	0.0542	± 0.0012	0.01946	± 0.000442	3130	33400	556118	461664	34482	250985	93648.65	11883	19698	4873	976	222	271	173	42.9	13.0	19.5
60	16.59	± 0.38	0.0540	± 0.0012	0.01944	± 0.000447	3270	30600	567511	450245	322948	245733	111283.8	13884	23819	5986	1524	323	445	236	36.4	16.8	19.5
61	16.55	± 0.42	0.0537	± 0.00124	0.01905	± 0.00045	1860	69500	540928	433931	309267	224508	87702.7	12256	16683	3518	752	174	209	156	36.4	6.8	13.4
62	16.14	± 0.40	0.0538	± 0.00114	0.0194	± 0.000517	3700	34000	573325	481240	346883	233260	114189.2	14760	25226	6288	1467	359	498	232	72.1	27.3	32.5
63	16.35	± 0.38	0.0539	± 0.00121	0.01971	± 0.000462	2030	32300	582700	477977	342672	245733	13464	18894	4343	967	227	255	166	38.9	36.6	8.9	
64	16.45	± 0.44	0.0554	± 0.00135	0.01954	± 0.000525	1700	32600	584388	461664	345095	228665	100000	12398	22010	5457	1248	287	397	194	44.9	22.4	14.2
65	16.59	± 0.40	0.0538	± 0.00132	0.01921	± 0.00047	1476	33600	602532	453507	372845	246827	88648.65	12007	18794	4609	988	210	277	182	65.2	19.9	13.8
66	16.37	± 0.41	0.0588	± 0.00127	0.01931	± 0.000483	1900	42200	518987	451876	314635	231072	82297.3	12575	16432	3449	833	164	212	144	8.9	17.4	0.0
67	16.36	± 0.40	0.0541	± 0.00114	0.01942	± 0.000473	2520	30700	554008	451876	355603	263020	1112702.7	15293	23266	5789	1362	313	401	203	46.6	21.7	19.1
68	16.58	± 0.40	0.0536	± 0.00114	0.01947	± 0.000486	4360	30500	551055	445351	365302	253611	106891.9	12835	21859	5180	1167	253	342	175	54.3	10.6	2.8
69	16.48	± 0.36	0.0544	± 0.00126	0.01949	± 0.000443	2458	38700	52100	474715	376078	270460	98175.68	12860	19598	4571	1020	230	319	166	40.5	14.3	13.0
70	16.53	± 0.39	0.0532	± 0.00121	0.01939	± 0.00046	2109	32100	576371	450408	367457	266521	106081.1	13606	20251	4535	1053	232	317	178	28.3	21.7	0.0
71	16.45	± 0.44	0.0542	± 0.00132	0.01924	± 0.00052	1890	47100	562447	438825	335129	282079	98310.81	12877	19246	4321	959	221	321	186	34.0	13.7	19.1
72	16.48	± 0.42	0.0544	± 0.00118	0.01953	± 0.000499	1660	34700	583986	491028	385756	286433	96013.51	13819	19749	4488	1179	283	364	203	44.5	15.5	8.5
73	16.27	± 0.40	0.0557	± 0.00123	0.01927	± 0.000501	1970	86900	597046	405057	315733	243107	8015.14	11545	15829	3389	813	159	214	136	31.6	16.1	11.8
74	16.18	± 0.41	0.0540	± 0.00127	0.01937	± 0.000484	2270	37100	594937	442088	334052	248578	89054.05	12078	18492	3853	833	192	251	157	15.0	16.8	13.4
75	16.17	± 0.38	0.0535	± 0.00122	0.01985	± 0.000489	2460	31100	580591	451876	365302	266740	116216.2	14174	23317	5568	276	394	232	255	26.1	14.6	8.9
76	16.11	± 0.38	0.0542	± 0.00126	0.01946	± 0.000452	1563	33400	582278	446892	348060	269147	10429.7	14121	20251	4479	984	219	271	175	22.3	9.3	8.9

Table 3_U-Th_Pb Zircon sorted by age

Spot	Location	U (ppm)	Th (ppm)	Th/U	$^{207}\text{Pb}/^{238}\text{U}$	2 σ	$^{206}\text{Pb}/^{238}\text{U}$	2 σ	$^{207}\text{Pb}/^{206}\text{Pb}$	2 σ	ρ	$^{207}\text{Pb}/^{235}\text{U}$ Age (Ma)	2 σ	$^{206}\text{Pb}/^{238}\text{U}$ Age (Ma)	2 σ	$^{207}\text{Pb}/^{206}\text{Pb}$ Age (Ma)	2 σ	Probability of concordance
3	Core	690	223	0.32	10.760	0.242	0.423	0.0093	0.184	0.004	-0.05	2502	9	2272	18	2691	6	0.91
72		495	22	0.04	10.230	0.273	0.421	0.0111	0.174	0.004	0.06	2455	16	2264	33	2596	6	0.92
82		280	136	0.48	9.840	0.281	0.403	0.0112	0.177	0.004	-0.36	2418	19	2183	36	2625	5	0.90
80		46	34	0.74	6.460	0.176	0.364	0.0095	0.128	0.003	-0.06	2039	17	1998	29	2065	8	0.98
40		62	40	0.64	6.390	0.182	0.358	0.0097	0.130	0.003	-0.31	2030	18	1974	31	2095	9	0.97
37		151	53	0.35	6.426	0.151	0.358	0.0082	0.131	0.003	-0.19	2035	11	1972	19	2107	7	0.97
44		100	109	1.09	6.100	0.193	0.356	0.0108	0.124	0.003	-0.14	1989	21	1960	38	2020	8	0.99
2	Rim	444	141	0.32	8.210	0.198	0.355	0.0082	0.168	0.003	-0.31	2256	12	1958	19	2542	4	0.87
5		70	102	1.47	5.854	0.150	0.342	0.0090	0.125	0.003	0.01	1957	15	1895	28	2035	9	0.97
28		878	74	0.08	7.890	0.218	0.334	0.0090	0.173	0.004	-0.07	2218	18	1858	30	2584	10	0.84
48		28	15	0.53	6.030	0.251	0.334	0.0137	0.130	0.003	-0.12	1976	32	1856	58	2098	15	0.94
32		101	49	0.49	5.867	0.153	0.333	0.0085	0.129	0.003	0.18	1956	14	1853	26	2080	10	0.95
18		49	19	0.38	5.977	0.155	0.321	0.0083	0.137	0.003	0.03	1975	16	1799	23	2184	12	0.91
4		677	299	0.44	5.659	0.146	0.316	0.0080	0.130	0.003	-0.30	1924	14	1767	24	2103	5	0.92
83		48	22	0.47	5.510	0.163	0.314	0.0093	0.127	0.003	0.10	1906	20	1762	34	2056	15	0.93
39		125	113	0.90	5.190	0.144	0.309	0.0082	0.122	0.003	-0.39	1849	17	1737	27	1987	9	0.94
49		403	115	0.29	6.840	0.196	0.307	0.0083	0.161	0.003	-0.10	2090	18	1732	29	2466	9	0.83
35		182	124	0.68	5.660	0.158	0.298	0.0078	0.138	0.003	-0.22	1924	17	1683	25	2204	13	0.87
51		304	97	0.32	5.366	0.145	0.297	0.0079	0.131	0.003	-0.13	1878	16	1676	26	2111	5	0.89
66		693	223	0.32	6.470	0.176	0.295	0.0079	0.158	0.003	-0.11	2041	17	1664	26	2433	5	0.82
21		587	251	0.43	5.019	0.124	0.294	0.0070	0.125	0.003	-0.25	1824	12	1663	19	2028	5	0.91
16		118	107	0.91	5.043	0.126	0.294	0.0071	0.125	0.003	-0.23	1826	13	1660	20	2032	9	0.91
65		407	6	0.02	4.481	0.111	0.270	0.0067	0.120	0.002	0.15	1730	11	1539	20	1956	5	0.89
1		52	36	0.70	4.496	0.129	0.266	0.0072	0.122	0.003	-0.26	1729	17	1524	24	1995	14	0.88
22		128	32	0.25	4.144	0.103	0.266	0.0065	0.115	0.002	-0.13	1663	12	1519	19	1881	10	0.91
24		166	71	0.43	4.140	0.154	0.260	0.0086	0.117	0.002	-0.72	1660	25	1490	35	1910	12	0.90
54		66	43	0.64	4.218	0.118	0.253	0.0070	0.121	0.003	-0.09	1677	16	1452	25	1975	13	0.87
81		80	47	0.59	4.091	0.115	0.246	0.0068	0.120	0.003	0.00	1652	16	1417	24	1960	12	0.86
23		71	51	0.71	4.060	0.162	0.244	0.0080	0.121	0.003	-0.50	1650	29	1406	33	1979	15	0.85
31		41	17	0.41	3.840	0.134	0.236	0.0072	0.118	0.003	-0.29	1600	23	1367	28	1931	16	0.85
38		48	27	0.56	2.564	0.088	0.214	0.0072	0.087	0.002	0.00	1289	20	1251	31	1372	20	0.97
58		463	39	0.08	3.354	0.099	0.210	0.0060	0.116	0.002	-0.39	1496	18	1228	23	1903	10	0.82
46		275	126	0.46	2.377	0.068	0.208	0.0059	0.082	0.002	-0.19	1235	15	1219	22	1252	8	0.99
50		321	114	0.35	3.216	0.091	0.205	0.0059	0.115	0.002	-0.13	1463	16	1202	23	1876	8	0.82
9		53	45	0.84	2.485	0.076	0.170	0.0049	0.106	0.002	0.04	1267	17	1011	20	1724	17	0.80
41		36	16	0.45	2.302	0.077	0.156	0.0052	0.107	0.003	0.07	1211	19	935	23	1754	23	0.77
45		65	29	0.45	2.113	0.072	0.153	0.0047	0.100	0.002	-0.17	1152	19	919	20	1620	18	0.80
30		270	29	0.11	1.994	0.083	0.146	0.0049	0.099	0.002	-0.73	1111	25	878	22	1607	20	0.79
78		157	40	0.26	1.241	0.040	0.111	0.0031	0.081	0.002	-0.30	818	14	677	13	1215	19	0.83
77		397	18	0.05	1.284	0.042	0.111	0.0033	0.084	0.002	-0.40	838	15	675	14	1287	10	0.81
73		238	34	0.14	1.054	0.042	0.097	0.0028	0.077	0.002	-0.57	730	17	597	12	1121	24	0.82
19		224	185	0.83	0.775	0.020	0.096	0.0024	0.060	0.001	0.00	582	8	589	9	585	15	1.01
14		264	120	0.45	0.744	0.020	0.092	0.0024	0.059	0.001	0.06	564	8	567	10	564	18	1.00
69		39	33	0.84	0.687	0.022	0.089	0.0022	0.056	0.001	0.07	531	10	552	8	466	40	1.04
64		409	196	0.48	0.708	0.019	0.089	0.0021	0.058	0.001	0.02	544	8	549	7	531	15	1.01
56		37	66	1.77	0.693	0.026	0.089	0.0025	0.057	0.002	-0.24	534	13	548	10	494	49	1.02
52		113	49	0.44	0.720	0.022	0.088	0.0023	0.060	0.001	0.08	550	9	546	9	591	23	0.99
43		119	68	0.57	0.716	0.022	0.088	0.0025	0.059	0.001	-0.04	548	10	544	11	567	22	0.99
60	Core	148	95	0.64	0.708	0.019	0.087	0.0021	0.059	0.001	0.17	545	8	540	7	559	24	0.99
57		119	117	0.99	0.709	0.019	0.086	0.0024	0.059	0.001	0.20	544	7	532	10	574	24	0.98
62		456	176	0.39	0.691	0.018	0.086	0.0022	0.058	0.001	-0.01	535	8	532	8	539	12	1.00
27		61	45	0.74	0.681	0.023	0.086	0.0025	0.058	0.002	0.21	527	11	532	11	522	39	1.01
68		66	47	0.71	0.695	0.023	0.086	0.0023	0.058	0.001	0.04	535	11	531	9	558	33	0.99
42		136	114	0.84	0.692	0.020	0.086	0.0023	0.059	0.001	-0.12	534	9	530	9	551	24	0.99
13		184	64	0.35	0.674	0.017	0.085	0.0020	0.058	0.001	0.29	523	7	526	7	523	24	1.01
6		1215	931	0.77	0.694	0.016	0.085	0.0019	0.060	0.001	0.09	535	5	524	5	588	9	0.98
55		215	71	0.33	0.681	0.020	0.085	0.0021	0.058	0.001	-0.21	527	9	523	8	549	16	0.99
33		82	69	0.84	0.667	0.019	0.085	0.0025	0.058	0.001	0.10	519	9	523	10	512	26	1.01
12		74	55	0.75	0.656	0.018	0.084	0.0020	0.057	0.002	0.12	512	8	520	6	468	40	1.02
74	Core	48	38	0.78	0.675	0.021	0.084	0.0023	0.058	0.002	-0.04	524	10	519	9	520	42	0.99
34		296	229	0.77	0.655	0.017	0.083	0.0020	0.057	0.001	0.04	512	7	511	7	498	16	1.00
63		122	804	6.59	0.674	0.021	0.082	0.0022	0.059	0.001	-0.03	523	10	510	8	577	29	0.97
47		173	2	0.01	0.637	0.018	0.081	0.0019	0.058	0.001	-0.03							

Table 4A_REE Zircon_McD_S sorted by age

Spot		U (ppm)	Th (ppm)	Hf (ppm)	La (ppm)	Dy (ppm)	Pr (ppm)	Nd (ppm)	Sm (ppm)	Eu (ppm)	Gd (ppm)	Tb (ppm)	Dy (ppm)	Ho (ppm)	Er (ppm)	Tm (ppm)	Lu (ppm)	Yb (ppm)	Th/U	Yb/Gd	Ce/Sm	Eu/Eu*	Ce/Gd	Lu/Dy	Ui/Ce
8	c (h)	937	352	1187.38	0.13	29.04	3.49	9.41	45.27	22.38	337	609	1451	2381	3575	4818	5839	6870	0.38	2953	0.18	2.66	0.47	53	
36	c (h)	1837	213	19262	97.47	234.91	360.99	678.34	1304.05	710.48	980	590	691	934	1188	1866	2845	4106	0.12	0.61	0.63	0.75	0.59	13	
15	r	224	30	113786	0.04	3.33	0.67	3.06	17.91	8.35	56	47	46	39	29	26	35	34	0.13	0.71	0.26	0.77	0.07	110	
59	c (h)	989	54	115728	0.38	7.01	3.60	8.71	46.49	57.19	128	115	83	79	62	56	52	50	0.05	0.75	0.75	0.75	0.63	0.05	230
25	r	325	23	117864	0.04	2.64	0.48	1.38	11.35	7.99	32	36	46	60	84	155	213	309	0.07	4.06	0.42	0.96	0.67	0.67	200
76	r	223	27	121068	0.03	2.95	0.91	2.74	15.81	14.39	38	51	57	49	54	69	86	106	0.12	1.63	0.59	0.77	0.19	0.19	123
79	r	272	15	114466	0.05	0.86	0.68	1.88	7.84	6.04	40	42	277	330	292	231	177	170	0.06	2.89	0.34	0.46	0.06	0.06	514
20	r	258	17	118447	0.02	2.20	0.60	1.77	9.59	6.75	43	75	142	258	375	607	807	935	0.06	40.48	0.33	0.95	0.66	0.66	191
17	c (s)	337	12	126214	0.06	1.89	0.52	1.53	6.22	4.97	46	74	208	383	625	1263	1870	2439	0.03	29.29	0.29	1.26	1.17	1.17	291
70	r	378	7	126117	0.08	1.45	0.10	0.96	5.07	3.91	27	111	271	463	689	927	1093	1179	0.02	17.14	0.33	1.19	0.44	0.44	425
53	m	253	8	123981	0.09	1.22	0.18	0.59	4.19	3.55	35	99	235	372	541	644	652	626	0.03	13.00	0.29	1.21	0.27	0.27	338
10	c (h)	393	91	104563	0.03	57.59	0.64	2.12	9.05	6.75	66	122	283	504	813	1316	1764	2480	0.23	17.39	0.28	26.34	0.88	0.88	11
29	m	261	11	116505	0.05	3.13	0.27	0.81	3.38	3.20	32	72	179	295	488	785	1075	1488	0.04	40.00	0.31	3.84	0.83	0.83	136
71	r	301	7	123204	0.13	2.76	1.83	4.16	7.64	4.44	35	136	326	562	938	1433	1820	2276	0.02	27.14	1.50	0.70	0.70	0.70	178
26	c (s)	125	103	94660	0.13	21.86	2.38	5.86	41.08	29.66	146	227	393	625	901	1239	1553	1976	0.02	6.39	0.38	2.20	0.50	0.50	9
11	c (h)	601	358	134456	0.05	36.87	1.93	4.60	36.89	23.09	143	211	427	647	1019	1615	2373	3215	0.60	4.89	0.32	4.14	0.75	0.75	27
7	c (b)	763	40	131553	0.87	9.15	10.13	11.36	28.78	28.60	106	165	404	661	1075	1822	2658	3374	0.06	9.80	0.52	1.32	0.83	0.83	136
67	c (h)	394	4	123230	0.05	0.46	0.50	1.86	7.50	1.60	60	199	313	348	369	340	314	350	0.01	15.00	0.08	0.25	0.11	0.11	1407
75	c (o)	222	5	119417	0.26	1.11	1.01	1.77	7.09	4.44	157	299	366	412	413	360	423	423	0.02	7.65	0.24	0.65	0.14	0.14	326
47	m	173	2	122921	0.05	0.17	0.05	0.42	5.20	3.02	43	124	247	229	193	186	182	199	0.01	8.67	0.20	0.14	0.08	0.08	1619
61	c (h)	166	25	102291	0.05	12.07	0.44	1.31	10.07	7.46	46	106	241	366	534	806	1118	1398	0.15	5.52	0.35	4.97	0.58	0.58	22
63	c (h)	122	804	22324	0.74	64.11	20.88	62.36	185.81	467.14	553	861	1191	1363	1688	2126	2193	2309	6.59	1.11	1.46	1.43	0.19	0.19	3
34	o	296	229	109515	0.06	112.07	0.55	2.19	18.51	10.48	116	249	524	1007	1506	2324	2869	3943	0.77	24.81	0.23	25.07	0.75	0.75	4
74	m	48	38	92427	0.08	14.71	0.56	1.53	7.57	16.16	56	121	267	445	749	1255	1714	1914	0.78	0.79	0.99	0.79	0.79	0.79	5
12	o	74	55	84175	0.05	19.90	1.48	3.63	20.34	11.90	75	112	241	443	608	915	1286	1537	0.75	7.50	0.30	4.05	0.64	0.64	6
55	c (o)	215	71	98915	0.04	16.66	0.60	175.05	14.73	10.83	67	152	303	496	875	1215	1553	2130	0.33	12.92	0.34	4.68	0.70	0.70	21
6	c (o)	1215	931	83883	0.33	85.32	22.41	34.14	175.00	78.51	799	1127	2130	3205	4256	5980	7205	8689	0.77	12.47	0.21	2.02	0.41	0.41	23
33	o	82	69	77184	0.13	57.10	2.70	10.09	53.31	79.40	335	715	1081	234	353	2725	3534	4634	0.84	7.16	0.71	4.44	0.65	0.65	2
13	c (o)	184	64	96602	0.01	14.68	0.51	1.20	11.08	8.88	72	122	262	487	719	1053	1503	1923	0.35	10.56	0.73	0.31	5.49	0.73	20
42	c (o)	136	114	70291	0.15	26.59	3.59	14.22	44.26	58.97	157	235	382	641	950	1547	2000	2642	0.84	6.67	0.71	2.49	0.69	0.69	8
68	c (o)	66	47	93981	0.07	23.00	0.38	2.41	8.65	11.55	39	97	172	262	478	652	842	1224	0.71	4.69	0.63	11.02	0.71	0.71	5
57	c (o)	119	117	74475	0.11	33.77	4.64	21.88	97.30	22.02	360	615	1085	1676	2350	2862	3385	3817	0.99	23.91	0.12	1.44	0.35	0.35	6
27	c (s)	61	45	90097	0.01	21.40	0.59	2.67	10.47	8.70	71	103	213	352	523	814	1056	1411	0.74	6.25	0.32	8.46	0.66	0.66	5
62	c (o)	456	176	98058	0.05	21.70	2.33	1.20	38.45	30.02	108	202	365	588	962	1421	2087	2907	0.39	4.62	0.47	2.34	0.80	0.80	34
60	m	148	95	93107	0.12	31.32	4.38	13.37	50.68	41.03	130	248	442	617	906	1360	1646	2150	0.64	6.22	0.51	2.56	0.49	0.49	8
43	c (o)	119	68	84466	0.05	11.00	0.75	3.94	22.77	27.18	77	152	326	496	773	1202	1559	2053	0.57	6.25	0.65	2.00	0.63	0.63	18
52	c (o)	113	49	10874	0.02	36.87	0.55	2.10	15.68	16.16	95	217	480	830	1400	2117	2844	4024	0.44	9.09	0.42	9.74	0.84	0.84	5
56	c (s)	37	66	90971	0.09	118.60	1.95	7.07	49.86	27.53	242	402	793	1201	1756	2275	2522	3256	1.77	13.41	0.25	9.89	0.41	0.41	1
64	c (o)	409	196	122136	0.05	45.35	0.86	3.41	20.27	1.78	101	224	480	835	1513	2275	2783	3638	0.48	30.00	0.04	9.27	0.76	0.76	15
69	c (h)	39	33	100583	0.01	19.90	0.66	1.82	12.16	14.03	57	121	226	374	623	834	1118	1553	0.84	5.25	0.53	6.78	0.69	0.69	3
14	c (o)	264	120	10835	0.01	27.08	1.31	2.47	11.35	3.91	72	116	253	449	688	1113	1404	1955	0.45	13.85	0.14	9.88	0.77	0.77	16
73	r	238	34	114369	0.09	10.28	1.86	4.97	21.62	15.81	75	189	447	575	810	901	1150	0.14	6.36	0.39	1.97	0.40	0.40	38	

Table 4B_Zircon_McD_S sorted by age

Spot	Description	U (ppm)	Th (ppm)	Hf (ppm)	La (ppm)	Ce (ppm)	Pr (ppm)	Nd (ppm)	Sm (ppm)	Eu (ppm)	Gd (ppm)	Dy (ppm)	Tb (ppm)	Ho (ppm)	Er (ppm)	Tm (ppm)	Yb (ppm)	Lu (ppm)	Th/U	Yb/Gd	Eu/Eu*	Ce/Sm	Lu/Dy	U/Ce		
19	0	224	185	100388	0.02	38.34	1.07	3.89	27.91	9.77	136	252	569	1004	1563	2413	3019	3813	0.83	34.50	0.16	5.69	0.67	10		
77	m	397	18	123010	0.38	3.07	1.47	3.00	19.12	12.43	74	158	205	203	248	331	400	423	0.05	2.48	0.33	0.66	0.21	211		
78	r	157	40	85631	0.18	11.75	1.50	1.95	6.01	11.19	28	53	89	121	238	416	573	907	0.26	3.62	0.86	8.09	1.02	22		
30	r(o)	270	29	110688	0.04	4.26	0.24	0.94	6.15	6.22	55	120	256	410	628	955	1137	1402	0.11	13.53	0.34	2.87	0.55	103		
45	c(s)	65	29	100971	0.05	7.94	0.17	1.05	9.32	8.35	26	66	132	194	333	474	609	793	0.45	6.19	0.54	3.53	0.60	13		
41	c(h)	36	16	94660	0.03	15.01	0.44	1.55	7.09	9.77	47	71	138	225	406	619	814	1061	0.45	8.64	0.53	8.76	0.77	4		
9	o	53	45	82718	0.03	35.73	1.76	4.99	21.35	13.68	101	129	269	434	569	789	1106	1358	0.84	7.62	0.30	6.93	0.50	2		
50	c(o)	321	114	97087	0.38	18.76	0.80	3.74	14.46	18.29	59	108	226	379	621	976	1205	1565	0.35	8.21	0.62	5.37	0.69	28		
58	c(o)	483	39	113010	0.30	4.32	1.37	2.47	15.54	14.92	59	124	200	273	375	502	632	850	0.08	2.94	0.49	1.15	0.43	175		
46	c(h)	275	126	105825	0.03	41.60	0.69	3.44	25.34	3.37	137	260	488	766	1288	1753	2112	2817	0.46	23.13	0.06	6.80	0.58	11		
38	c(s)	48	27	84078	0.05	13.51	1.23	4.46	22.50	9.59	107	174	341	549	869	1150	1547	2033	0.56	10.87	0.20	2.49	0.60	6		
31	m	41	17	108350	0.04	15.50	0.22	0.83	6.08	4.97	13	29	51	104	181	307	492	720	0.41	6.40	0.57	10.56	1.40	4		
22	c(h)	128	32	95728	0.01	1.75	0.68	2.52	9.59	1.15	26	23	54	61	102	136	167	199	0.25	8.14	0.07	0.75	0.37	119		
24	c(h)	166	71	117573	0.02	6.04	1.00	3.04	17.91	4.97	86	94	126	132	143	153	151	157	0.43	2.56	0.13	1.40	0.12	45		
407	c(s)	407	6	124078	0.02	0.44	0.29	0.88	13.58	2.13	89	216	261	213	239	201	213	239	0.02	3.55	0.06	0.13	0.09	1508		
65	c(s)	81	c(o)	80	47	79709	0.08	24.96	0.89	2.54	12.97	32.68	65	158	296	542	1025	1615	2348	3687	0.59	5.96	1.12	7.97	1.25	5
23	c(o)	71	51	90291	0.03	28.71	1.33	3.92	19.26	15.45	84	120	221	368	566	818	1236	1602	0.71	6.92	0.38	6.18	0.72	4		
54	m	66	43	97379	0.31	22.51	0.82	3.79	16.28	10.48	76	125	205	344	533	794	981	1329	0.64	5.45	0.30	5.73	0.66	5		
39	c(o)	125	113	92039	0.08	61.34	0.46	4.16	15.95	18.83	75	134	259	631	866	1261	1565	90	6.67	0.54	15.93	0.60	3			
1	c(s)	52	36	89126	0.22	88.33	74.39	75.75	50.00	54.05	97	213	346	534	798	1186	1602	2070	0.70	2.26	6.16	0.75	1	1508		
44	c(o)	100	109	83786	0.17	44.05	1.35	6.46	32.43	27.18	125	182	351	526	813	1097	1395	1772	1.09	5.43	0.43	5.63	0.50	4		
21	o	587	251	110194	0.04	20.39	0.71	1.88	9.59	5.51	54	96	198	379	609	1000	1311	1748	0.43	10.40	0.24	8.80	0.88	47		
16	c(o)	118	107	98835	8.02	83.20	86.21	78.77	76.35	27.89	118	124	251	425	660	1016	1478	2028	0.91	4.09	0.29	4.51	0.81	2		
5	m	70	102	97767	0.01	25.61	0.58	1.33	5.81	4.80	36	60	136	222	373	595	786	1183	1.47	9.33	0.33	18.26	0.87	4		
83	c(s)	48	22	81942	0.02	8.65	0.32	0.77	4.80	5.15	14	28	41	86	232	370	549	786	0.47	4.41	0.62	7.46	1.32	9		
80	c(s)	46	34	98738	0.04	30.67	0.41	1.47	9.66	8.70	46	85	150	256	424	725	888	1240	1748	0.74	7.08	0.41	13.15	0.83	2	
32	o	101	49	103010	0.27	49.92	0.69	3.15	10.07	7.28	36	71	123	229	406	704	1075	1488	0.49	13.75	0.38	20.54	1.21	3		
40	m(s)	62	40	89709	0.02	34.26	0.56	2.04	12.84	13.85	64	94	185	302	483	704	1025	1329	0.64	3.87	0.48	11.05	0.72	3		
48	c(s)	28	15	91563	0.03	13.88	0.53	1.09	3.45	6.04	21	35	74	100	194	285	395	630	0.53	3.15	0.72	16.69	0.86	3		
677	c(h)	299	110194	0.01	21.04	0.66	1.40	4.80	9.59	72	140	327	579	1025	1595	2329	3443	1411	0.32	1.18	9.08	2.17	0.05	52		
37	c(s)	151	53	94951	0.01	12.02	0.64	1.68	13.85	6.22	87	170	343	661	1150	1947	3610	4386	0.35	13.85	0.18	6.59	1.05	11		
51	c(o)	304	97	107767	0.21	6.82	0.72	2.76	16.96	3.91	71	145	273	480	800	1089	1509	2167	0.11	1.67	0.11	0.79	0.73	288		
18	c(o)	49	19	91553	0.05	10.77	0.73	1.01	9.12	5.51	42	80	186	344	500	846	1081	1439	0.38	17.33	0.28	4.89	0.77	7		
35	o	182	124	99515	0.08	3.38	0.53	2.54	13.31	4.09	68	98	170	260	328	478	522	679	0.68	10.00	0.14	1.05	0.40	88		
66	c(o)	633	223	106899	0.23	16.97	1.29	4.75	17.16	44.23	59	116	204	352	580	781	1081	1411	0.32	2.17	0.49	9.09	0.69	67		
49	c(o)	403	115	129822	0.11	2.28	0.54	2.01	20.07	1.74	93	161	232	251	306	348	397	438	0.29	11.58	0.04	0.47	0.17	288		
2	r	444	141	105728	0.09	8.40	1.38	2.54	15.68	7.82	90	129	267	425	611	899	1118	1610	0.32	8.18	0.21	2.22	0.60	86		
28	c(h)	878	74	98350	0.48	11.97	4.04	6.48	16.82	8.88	35	61	97	171	259	445	646	878	0.08	7.78	0.37	2.95	0.90	120		
72	r	495	22	110194	0.03	7.26	0.39	0.61	4.73	3.37	34	65	145	229	432	700	984	1504	0.04	16.92	0.27	6.36	1.04	111		
82	c(b)	280	136	128029	0.07	3.34	0.82	3.22	22.16	2.49	76	151	215	242	269	308	289	300	0.48	9.17	0.06	0.63	0.12	137		
3	c(h)	690	223	96505	0.10	12.72	2.78	7.72	48.58	15.28	233	280	577	837	280	259	322	10.91	0.14	1.08	0.05	0.51	88			